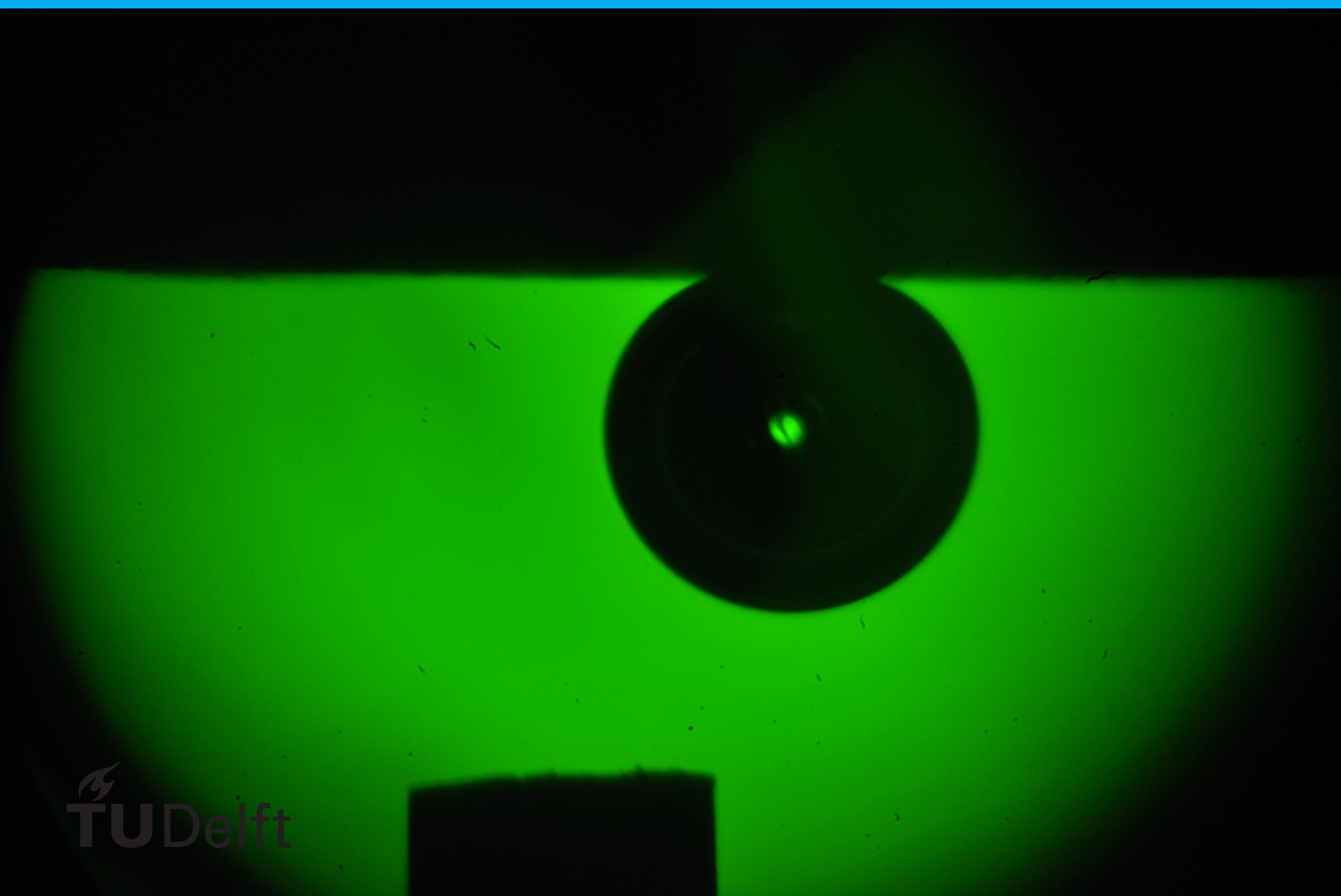


# Static Contact Angle Measurements

for Subsurface  
Hydrogen Storage

Wuis Glerum





# Static Contact Angle Measurements

**for Subsurface  
Hydrogen Storage**

by

Wuis Glerum

to obtain the degree of Master of Science  
at the Delft University of Technology,  
to be defended publicly on Tuesday September 14, 2021 at 14:00 AM.

Student number: 4350219  
Project duration: December 1, 2020 – September 14, 2021  
Thesis committee: Dr. H. Hajibeygi, TU Delft, main supervisor  
Dr. R. Farajzadeh, TU Delft, co-supervisor  
Dr. P. Boukany, TU Delft

An electronic version of this thesis is available at <http://repository.tudelft.nl/>.



# Abstract

Hydrogen storage in porous media is a potential solution to the energy distribution problems we might face in the future. Intermittent energy sources such as solar and wind energy need to be accompanied with temporary energy storage to accommodate the times when production and demand do not match. Hydrogen is an energy carrier with a large mass energy density as it can be made completely green through electrolysis and it will not release greenhouse gases when used to produce energy through combustion process. However it has to be stored in large enough volumes to reach the required energy demand. The storage can be done in the subsurface in either aquifers, depleted hydrocarbon reservoirs or salt caverns which are giant porous or cave volumes available to store compressed gases.

At this moment, there is a lack of knowledge for safe and efficient hydrogen storage at reservoir (continuum cm and above) scale and pore scale (micrometer-scale). In a reservoir model the relative permeability and capillary pressure are key parameters to characterise flow behaviour and capacity. These are upscaled parameters we can find through pore-network modelling, among other approaches. For a pore-network model, the contact angle and accompanying wettability characteristics (i.e., interfacial tension) are important to obtain reliable upscaled functions and parameters.

Through the use of a captive bubble method, in this thesis work, we have been able, for the first time, to characterize the contact angle of a hydrogen/brine/rock system at different pressures, temperatures, salinity's and rock compositions. It was found that the contact angle of a hydrogen/brine/rock system is in the range of between 21.1 and 43 degrees. Moreover, for the studied range of varying parameters, the contact angle stayed remained relatively constant. The results of this study are published in the Journal of Advances In Water Resources (<https://doi.org/10.1016/j.advwatres.2021.103964>).



# Preface

This thesis is written as a part of obtaining the Master title in Geo-Energy engineering. I've started this project thinking I would be operating an experimental setup for a few months and then moving to pore network modelling with the results from the experiments. However, I have learned that experiments do not always go how you would expect them to go. Through the first months of working on my thesis, the experimental work was more than imagine and took over the whole thesis.

I want to thank Hadi Hajibeygi for giving me the opportunity to do experimental work as a large part of my thesis. Thank you to Leila Hashemi for the daily supervision and help for the experiments and writing of my thesis. A large thanks to Michiel Slob, the lab technician being there everyday to repair the setup, make changes and keeping me on track during the project. Thank you to Rouhi Farajzadeh for the weekly meetings and his expertise on experimental work and lastly to Sian Jones for being around the lab and her general help throughout the months in the lab.

*Wuis Glerum  
Delft, September 2021*



# Contents

<b>List of Figures</b>	<b>ix</b>
<b>List of Tables</b>	<b>xi</b>
<b>Nomenclature</b>	<b>xiii</b>
<b>1 Introduction</b>	<b>1</b>
1.1 Energy Storage . . . . .	1
1.2 Hydrogen Storage . . . . .	2
1.3 Pore Scale Interaction . . . . .	2
<b>2 Theory</b>	<b>5</b>
2.1 Contact Angle. . . . .	5
2.2 Dynamic Contact Angle . . . . .	6
2.3 Capillary Pressure . . . . .	6
2.4 Relative Permeability. . . . .	7
2.5 Measuring Technique. . . . .	8
2.5.1 Sessile drop. . . . .	8
2.5.2 Captive bubble . . . . .	8
2.5.3 Tilted plate . . . . .	8
2.5.4 Tilting plate . . . . .	8
2.5.5 Wilhelmy balance. . . . .	9
2.5.6 Capillary tube . . . . .	9
2.6 Surface Roughness . . . . .	9
<b>3 Experimental setup and procedures</b>	<b>11</b>
3.1 Captive Bubble Setup . . . . .	11
3.2 Materials . . . . .	11
3.3 Procedure. . . . .	12
3.4 Image Analysis . . . . .	12
3.5 Setup Calibration . . . . .	14
3.6 Experimental Conditions . . . . .	15
3.6.1 Experimental time . . . . .	15
<b>4 Results and Discussion</b>	<b>17</b>
4.1 Bubble Size . . . . .	17
4.2 Pressure and Temperature. . . . .	17
4.3 Salinity . . . . .	18
4.4 Rock Type . . . . .	19
4.5 Experiment Discussion. . . . .	19
4.5.1 Rock Alteration . . . . .	19
4.5.2 Surface Roughness . . . . .	20
<b>5 Conclusions</b>	<b>21</b>
5.1 Further Research and Outlook. . . . .	21
<b>6 Technical Challenges</b>	<b>23</b>
6.1 Aged Rock Samples . . . . .	23
6.2 Methane and Methane-Hydrogen Mixtures . . . . .	23
6.2.1 Experimental Discussion. . . . .	23

---

6.3	Captive Bubble Setup Performance . . . . .	24
6.3.1	Nozzle. . . . .	24
6.3.2	Gas Line Volume . . . . .	24
6.3.3	Images . . . . .	25
6.3.4	Rock replacement . . . . .	26
6.3.5	Flushing Mechanism . . . . .	26
	<b>Bibliography</b>	<b>27</b>
<b>A</b>	<b>Rock sample surface properties</b>	<b>31</b>
<b>B</b>	<b>Measurements</b>	<b>35</b>
B.1	Hydrogen/Brine/Bentheimer . . . . .	35
B.2	Hydrogen/Brine/Berea . . . . .	36
B.3	Hydrogen/Brine/Edwards White . . . . .	37
<b>C</b>	<b>Densities</b>	<b>39</b>
<b>D</b>	<b>Scanning Electron Microscope Data</b>	<b>43</b>

# List of Figures

1.1	Hydrogen storage during high renewable energy production (1) to be used during periods of high demand and low renewable energy production. (Heinemann et al., 2021) . . . . .	1
2.1	Schematic of contact angles measured of water in a oil/water system. The contact angle ( $\theta$ ) is measured as the angle between the surface water-line and the water-oil line. When the contact angle in this case is less than $90^\circ$ the surface is water-wet. When the angle is larger than $90^\circ$ the surface is oil-wet (Blunt, 2017). . . . .	5
2.2	Schematic of the acting surface tension forces $\gamma$ and the contact angle $\theta$ . . . . .	6
2.3	Schematic of the Capillary tube (Anderson, 1987b) . . . . .	7
2.4	Relative permeability curves for oil (a) and water (b) for different contact angles (Bradford et al., 1997) . . . . .	7
2.5	Schematic of the Tilted Plate method by Macdougall et al., (1942) . . . . .	8
2.6	Schematic of the Tilting Plate method (Yuan and Lee, 2013) . . . . .	9
2.7	Schematic of the Wilhelmy balance method (Yuan and Lee, 2013) . . . . .	9
3.1	Schematic of the experimental setup of the captive bubble cell . . . . .	12
3.2	Three dimensional view of a berea rock surface through the Leica 3D microscope. The sample has a $P_a$ factor of 0.03 mm. Blue, red and green lines give the x,y and z directions used to determine the $P_a$ value. . . . .	12
3.3	Hydrogen bubble image taken at a 5000ppm brine, 70.2 bar and $22.3^\circ\text{C}$ with a Berea sandstone. The bubble and nozzle can be clearly differentiated in black from the brine in green. The flat surface at the top corresponds to the rock surface . . . . .	13
3.4	Image analysis process to determine the contact angle from the original image (1) to the fitted bubble profile (5) by Hashemi et al., May 2021 . . . . .	13
3.5	Schematic of an axisymmetric drop, modified after Li et al., 1992 . . . . .	14
4.1	Effect of bubble size in the system of hydrogen/water/bentheimer $23.5^\circ\text{C}$ and 51.2bar. A shows the volume change over time and b the corresponding reported contact angles (Hashemi et al., May 2021) . . . . .	17
4.2	Measured static contact angle of hydrogen for a bentheimer sandstone in pure water (a) and 5000 ppm brine (b) at varying pressure and temperature from 3.2 . . . . .	18
4.3	Measured static contact angle of hydrogen for a bentheimer sandstone in different brines from Table 3.2 at close to $30^\circ\text{C}$ . . . . .	18
4.4	Measured static contact angle of hydrogen for a bentheimer sandstone, Berea sandstone and Edwards White Limestone in pure water . . . . .	19
4.5	Bentheimer sample with a changed color after experimentation . . . . .	20
6.1	Saturation vessel at a pressure of 100 bar with rock samples in oil . . . . .	24
6.2	Hydrogen bubble with a saturated bentheimer sandstone attached to the PEEK nozzle .	25
6.3	Hydrogen bubble image taken at a 5000ppm brine, 71.1 bar and $32.7^\circ\text{C}$ with a Bentheimer sandstone. . . . .	26
A.1	Bentheimer sandstone used during the repeat test with hydrogen . . . . .	31
A.2	Berea sandstone used during the initial test with hydrogen . . . . .	32
A.3	Edwards White limestone used during the initial test with hydrogen . . . . .	32
A.4	Bentheimer sandstone used during the initial test with methane and methane-hydrogen mixtures . . . . .	33
A.5	Bentheimer sandstone used during the repeat test with methane and methane-hydrogen mixtures . . . . .	33

---

D.1	Pore scale image of a bentheimer sandstone before usage in the experiment . . . . .	43
D.2	Pore scale image of a berea sandstone before usage in the experiment . . . . .	44
D.3	Pore scale image of an edwards white limestone before usage in the experiment . . . . .	44
D.4	Pore scale image of a bentheimer sandstone after usage in the experiment . . . . .	45
D.5	Pore scale image of a berea sandstone after usage in the experiment . . . . .	45

# List of Tables

3.1	Parameter comparison of the calibration of the setup . . . . .	15
3.2	Experimental conditions used during the Hydrogen/Brine/Rock experiment . . . . .	15
6.1	Different test cases used throughout the experiment for a Methane/brine/rock and Methane-Hydrogen/Brine/Rock systems . . . . .	25
A.1	Surface roughness values measured using the Leica 3D stereo explorer . . . . .	31
B.1	Contact angle values of hydrogen/pure water/Bentheimer. . . . .	35
B.2	Contact angle values of hydrogen/brine (5000 ppm NaCl)/Bentheimer. . . . .	35
B.3	Contact angle values of hydrogen/brine (50,000 ppm NaCl)/Bentheimer. . . . .	36
B.4	Contact angle values of hydrogen/pure water/Bentheimer, repeated tests. . . . .	36
B.5	Contact angle values of hydrogen/brine (5000 ppm NaCl)/Bentheimer, repeated tests. . . . .	36
B.6	Contact angle values of hydrogen/pure water/Berea. . . . .	36
B.7	Contact angle values of hydrogen/pure water/Berea, repeated tests. . . . .	37
B.8	Contact angle values of hydrogen/pure water/Edwards White . . . . .	37
B.9	Contact angle values of hydrogen/brine (5000 ppm NaCl)/Edwards White . . . . .	37
C.1	Density values used to calculate the contact angle for bentheimer sandstone . . . . .	40
C.2	Density values used to calculate the contact angle for berea sandstone . . . . .	41
C.3	Density values used to calculate the contact angle for bentheimer sandstone,repeat . . . . .	42
D.1	SEM data of a bentheimer sandstone before usage in the experiment . . . . .	43
D.2	SEM data of a berea sandstone before usage in the experiment . . . . .	43
D.3	SEM data of an edwards white limestone before usage in the experiment . . . . .	44
D.4	SEM data of an bentheimer sandstone after usage in the experiment . . . . .	44
D.5	SEM data of an berea sandstone after usage in the experiment . . . . .	46



# Nomenclature

$\gamma$	Interfacial Tension
$\rho$	Density
$\theta$	Contact angle
$\theta_a$	Advancing contact angle
$\theta_i$	Intrinsic contact angle
$\theta_r$	Receding contact angle
$g$	Gravitational acceleration
gl	Gas-Liquid interface
$P_c$	Capillary pressure
$P_{NW}$	Pressure of the non wetting phase
$P_{WET}$	Pressure of the wetting phase
$R$	Radius of curvature
$r_t$	Radius of the tube
$s$	arc length
sg	Solid-Gas interface
sl	Solid-Liquid interface
$z$	Height



# Introduction

The continuous increase of renewable energy sources like solar and wind energy gives several new challenges to solve. One of this is the intermittency of these energy sources, which makes balancing production and demand more challenging. At the beginning of June 2021 Dutch energy network provider Tennet announced that during a predictable solar eclipse there could be energy shortages (Schelfaut, 2021). This problem could become even larger as the relative share of solar energy production increases. Solar eclipses will not be the only challenges in energy shortages that we could face in the coming decades. Renewable energy production is dependent on seasonal fluctuations and atmospheric events, as seen in the resultant sunlight intensity or wind force (Heinemann et al., 2021). Meanwhile the demand can fluctuate due to warm summers or extremely cold winters. These different fluctuations mean that renewable energy is not able to satisfy the energy demand continuously.

## 1.1. Energy Storage

The solution to these fluctuations in renewable energy production would be the storage of excess energy during times of overproduction of energy see Figure 1.1. There are several ways in which

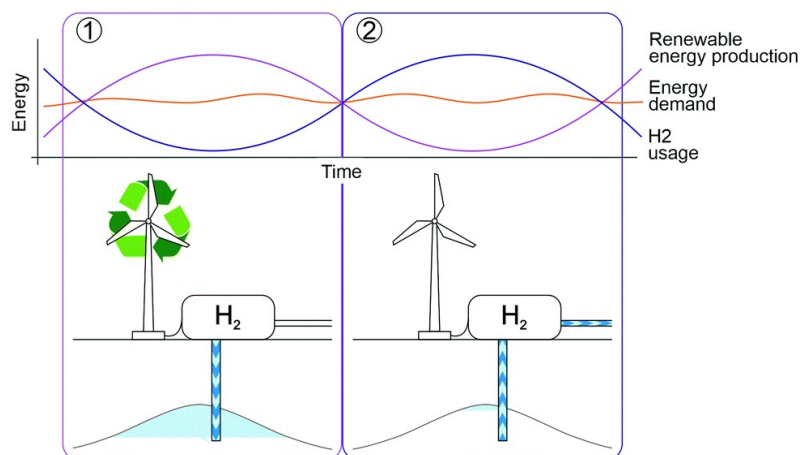


Figure 1.1: Hydrogen storage during high renewable energy production (1) to be used during periods of high demand and low renewable energy production. (Heinemann et al., 2021)

energy can be stored (batteries, gas cylinders and subsurface gas storage), but the required volumes of energy to keep cities and countries running leaves us with only subsurface gas storage as a viable option (Zivar et al., 2021). In the Netherlands, there are four porous medium storage sites operating with natural gases (RVO, 2019). Eventually, the production of greenhouse gases in our energy production chain should be minimized, to replace the current fossil fuel sources with low-carbon sources such as hydrogen. This gives us two requirements for a gas to be useful as energy storage.

1. Energy production capacity close to or exceeding natural gases
2. No production of greenhouse gases during production or conversion

Hydrogen gas closely satisfies both requirements. 1 m<sup>3</sup> of hydrogen produces 12.7MJ of energy, compared to 40MJ for methane (Zivar et al., 2021). The energy production comes from the combustion of hydrogen according to the following reaction equation  $\frac{1}{2} \text{H}_2 + \text{O}_2 = \text{H}_2\text{O}$ . This is only for the energy production phase of hydrogen. The production of the hydrogen itself would need to be free of greenhouse gas emission. This can be done through electrolysis which is known as 'green hydrogen' (Heinemann et al., 2021). Even hydrogen production through the use of hydrocarbons with carbon capture and storage, 'blue hydrogen', can help reduce emissions.

## 1.2. Hydrogen Storage

Experience with the storage of hydrogen is very limited (Zivar et al., 2021). There are not yet any real world projects which have been performed with pure hydrogen. Instead only mixtures with town gas or methane have been stored in a field. However, we can use some of our knowledge obtained from the experience of natural gas, compressed air and CO<sub>2</sub> storage. The storage locations for these gases are in salt caverns, aquifers and depleted hydrocarbon reservoirs (Dusseault et al., 2004, Eccles et al., 2009). These would also be prime locations for hydrogen storage. Even though there is a lot of information available on other gases, hydrogen has its own physical and chemical properties, which affect storage potential, especially in porous media (Juez-Larré et al., 2019, RVO, 2019).

Potential storage reservoirs are heterogeneous, consisting of different rock types and structures. Therefore, Continuous injection and production of hydrogen in porous media gives a multiphase problem, where both the fluid and the rock properties are required to understand the behaviour. The fluid-fluid and fluid-rock interactions are also present in these multiphase problems. When we understand these properties and interactions we can build models to predict the flow behaviour and storage capacities for hydrogen.

Accurate reservoir scale models rely heavily on two properties. These are the relative permeability of the fluids and the capillary pressure. The relative permeability describes the effective permeability of a specific fluid relative to the absolute permeability, where the effective permeability is the apparent permeability given to a fluid in a multiphase system (Honarpour and Mahmood, 1988). The capillary pressure describes the pressure required for a pore to be saturated by a different fluid from the fluid present in the pore (Brown, 1951). Both the relative permeability and capillary pressure are strongly affected by the wettability of the rock, which is a pore scale phenomenon (Anderson, 1987b), dependent on geochemistry (Larter and Aplin, 1995). The wetting behaviour of a rock and the accompanying relative permeability and capillary pressure curves, can, therefore be determined using a pore scale model.

## 1.3. Pore Scale Interaction

The pore network modelling by Hashemi et al., April, 2021 shows that the contact angle of hydrogen in a multiphase system is of crucial importance. The contact angle affects wetting behaviour and therefore the capillary pressure and relative permeability of a hydrogen system.

At this time, only two experimental studies are known that measure the contact angle. The first study is a core flooding experiment by Yekta et al., 2018. at [50 bar, 20°C] and [100 bar, 45°C] which finds the receding contact angle 21.56° and 34.9°, respectively. However, this has been calculated from their findings of the capillary pressure and relative permeability curves and not measured directly.

The second experiment by Iglauer et al., 2021 for pressures between 20 and 250 bar and temperatures of 296 to 343K on pure quartz, and shows the effect of both pressure and temperature on the contact

angle.

Based on the conclusions by Hashemi et al., (2021) that the contact angle are of great importance to pore scale modelling, wset out to find the missing knowledge about the static contact angle of hydrogen in a hydrogen/brine/rock system.



# 2

## Theory

To be able to understand the conclusions of Hashemi et al., (April, 2021), we need to understand what the contact angle defines, how it impacts reservoir production and what the relation is to the upscaled parameters of capillary pressure and relative permeability. In this chapter the theory behind the contact angle, wettability and its impact on the upscaled parameters will be explained. The chapter will also contain information on how contact angle measurements have been performed in the past, as well as the key parameter of surface roughness which affects this measurement the most.

### 2.1. Contact Angle

The contact angle is a measure of the wettability of a system as can be seen in Figure 2.1 (Morrow, 1990). The wettability of a system indicated to which phase present in the three phase system the surface is wetting, which is a significant issue in multiphase problems. The wettability of a reservoir

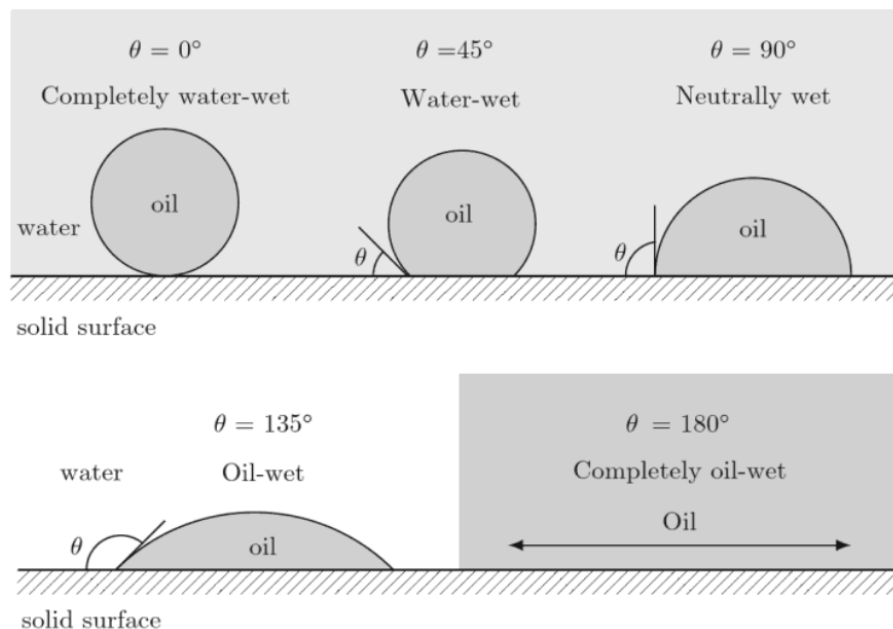


Figure 2.1: Schematic of contact angles measured of water in a oil/water system. The contact angle ( $\theta$ ) is measured as the angle between the surface water-line and the water-oil line. When the contact angle in this case is less than  $90^\circ$  the surface is water-wet. When the angle is larger than  $90^\circ$  the surface is oil-wet (Blunt, 2017).

is determined by complex interface boundary conditions acting within the pore space of the rocks (Morrow, 1990). Wetting behaviour is determined by the surface of the pores which are known to be

extremely complex. Mineral composition, surface roughness, pore geometry and adsorption effect can all be expected to influence wetting (Morrow, 1975). Due to these complexities we cannot expect the measured contact angle to be of a single value. However, the contact angle is a fundamental property of the system, referred to as the intrinsic contact angle ( $\theta_i$ ). The contact angle is related to the interfacial tension  $\gamma$  acting at the three phase line of contact by the Young's equation shown in Figure 2.2 (Morrow, 1975)

$$\gamma_{sg} = \gamma_{sl} + \gamma_{gl} \cos(\theta), \quad (2.1)$$

where  $_{sg}$  denotes the solid-gas interface,  $_{sl}$  the solid-liquid interface,  $_{gl}$  the liquid-gas interface and  $\theta$  the contact angle.

However wetting is not always a static state (Yuan and Lee, 2013), therefore it cannot always be

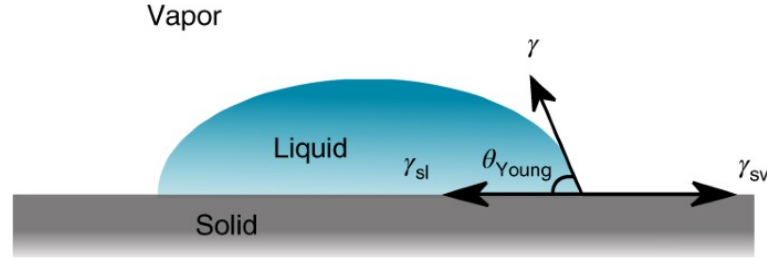


Figure 2.2: Schematic of the acting surface tension forces  $\gamma$  and the contact angle  $\theta$

described by a static contact angle.

## 2.2. Dynamic Contact Angle

When the system is in motion and the location of the three phase contact line moves, the system can be described by the dynamic contact angle. The dynamic contact angle is divided into the advancing ( $\theta_a$ ) and receding ( $\theta_r$ ) contact angle. The receding and advancing contact angles describe the system during drainage, when the non-wetting fluid displaces the wetting fluid, and its reverse, imbibition, respectively. The difference between the advancing and receding contact angle is called hysteresis. Hysteresis in the contact angle, also causes hysteresis in the capillary pressure (Anderson, 1987b). Therefore capillary pressure curves are always described for both drainage and imbibition.

## 2.3. Capillary Pressure

Capillary pressure is defined as the pressure difference across any fluid surface, a result of to free surface energy (Evans and Guerrero, 1979). In a storage reservoir this would correspond to the pressure difference between hydrogen and brine.

The pressure difference across the fluid-gas interface can be defined by the Young-Laplace equation (Blunt, 2017) as

$$P_c = \gamma \left( \frac{1}{R_1} + \frac{1}{R_2} \right), \quad (2.2)$$

where  $\gamma$  is the interfacial tension  $R_1$  and  $R_2$  are the radii of curvature of the interface and  $P_c$  is the capillary pressure which is defined as

$$P_c \equiv p_{NW} - p_W, \quad (2.3)$$

where  $p_{NW}$  is the pressure in the non wetting fluid and  $p_W$  is the pressure in the wetting fluid.

In a reservoir the radii of curvature are determined by the pore geometry, wettability, saturation and saturation history (Anderson, 1987b). To understand the capillary pressure at static conditions we can look at a capillary tube, as seen in Figure 2.3. When the radius of the tube ( $r_t$ ) is small, the curvature can be approximated by the curvature of a sphere with radius  $r_s$ . Because the tube is circular, the radii from equation 2.2 are equal to  $r_s$ . The relation between  $r_t$  and  $r_s$  is

$$\frac{r_t}{r_s} = \cos \theta. \quad (2.4)$$

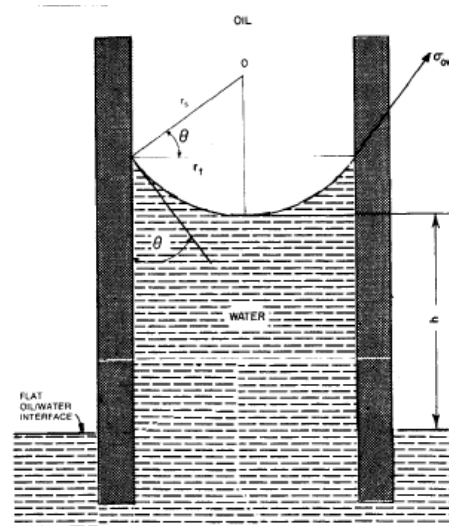


Figure 2.3: Schematic of the Capillary tube (Anderson, 1987b)

Substituting this into equation 2.2 the equation relating the contact angle to the capillary pressure, becomes

$$P_c = \frac{2\gamma \cos \theta}{r_t} \tag{2.5}$$

When describing the capillary pressure in a reservoir simulation, a capillary pressure curve is used. A capillary pressure curves describes the pressure required for a fluid to invade the rock to reach a certain saturation (Brown, 1951).

### 2.4. Relative Permeability

The relative permeability is a direct measure of the ability of the porous system to conduct one fluid when one or more fluids are present (Anderson, 1987a). The relative permeability of a porous medium is effected by the shapes of the pores, wettability, fluid distribution and saturation history. Through experiments it has been shown that the contact angle has a large effect on the relative permeability of the fluids as can be seen in Figure 2.4 (Owens and Archer, 1971) with similar results found through modelling (Bradford et al., 1997). Figure 2.4 shows that a change the contact angle of 45° can change the relative permeability by 10 percentage points.

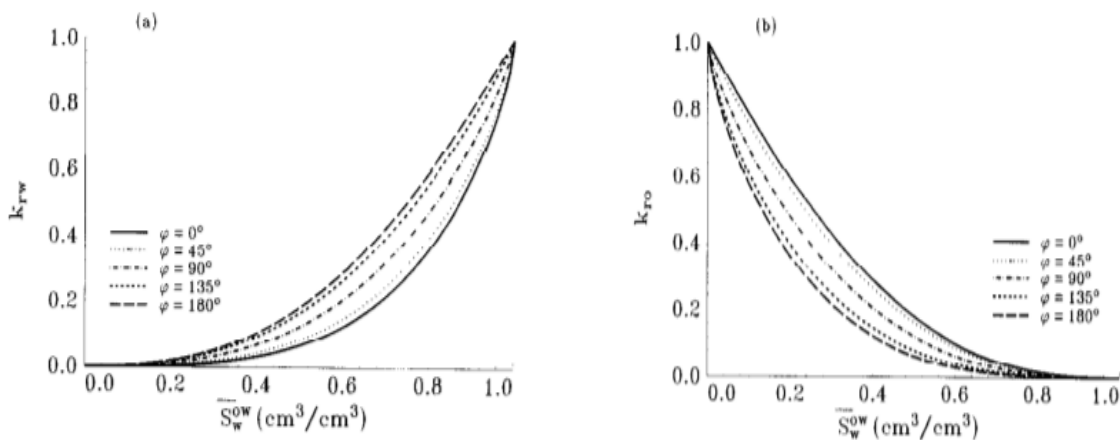


Figure 2.4: Relative permeability curves for oil (a) and water (b) for different contact angles (Bradford et al., 1997)

## 2.5. Measuring Technique

Several methods exist to measure both the static and dynamic contact angle. The following methods are commonly used (Yuan and Lee, 2013):

1. Sessile drop
2. Captive bubble
3. Tilted plate
4. Tilting plate
5. Wilhelmy balance
6. Capillary tube

### 2.5.1. Sessile drop

The sessile drop method is the most widely used method to determine the static contact angle. In this technique a liquid drop is placed on a flat solid surface, as seen in Figure 2.2. From the side of the drop a photograph is made, which can be used to determine the contact angle. As Yuan and Lee, (2013) suggest, the sessile drop method can best be done in an enclosed space, where the pressure can be regulated and airborne contamination is excluded.

### 2.5.2. Captive bubble

The captive bubble method can be seen as the inverse of the sessile drop method measuring the static contact angle. In the captive bubble method, a gas drop is released onto the bottom of a solid surface which is submerged in a liquid. Again, a photograph of the bubble is taken, which is analysed to determine the contact angle. Since temperature and pressure are easier to stabilize in larger a liquid volume, the captive bubble method is preferred for studying effects of temperature and pressure (Hashemi et al., May 2021).

### 2.5.3. Tilted plate

A modification to the sessile drop and captive bubble method, known as the tilted plate method can be made to find the dynamic contact angles by, as seen in Figure 2.5 (Macdougall et al., (1942)). The plate from the sessile drop method is tilted to find a  $\theta_{max}$  and  $\theta_{min}$  which would correspond to the advancing and receding contact angle. However this relationship must be used with caution as these are not always the same. This modification to the captive bubble method is not frequently used as the captive bubble method is much more sensitive and unstable to changes that alter the surface direction.

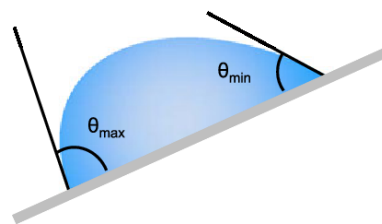


Figure 2.5: Schematic of the Tilted Plate method by Macdougall et al., (1942)

### 2.5.4. Tilting plate

The tilting plate method is used to measure the static contact angle. A plate is rotated to the liquid surface, as shown in Figure 2.6. The end of the plate is submerged until the meniscus at the plate boundary is horizontal. The angle between the surface and plate is the reported contact angle, as seen in Figure 2.6

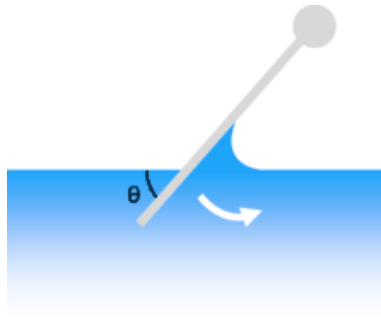


Figure 2.6: Schematic of the Tilting Plate method (Yuan and Lee, 2013)

### 2.5.5. Wilhelmy balance

A method for studying the dynamic contact angle is the wilhelmy balance method, see Figure 2.7. A solid plate is pushed or pulled into a liquid. The measured contact angle during this motion corresponds to the advancing and receding contact angle, respectively.

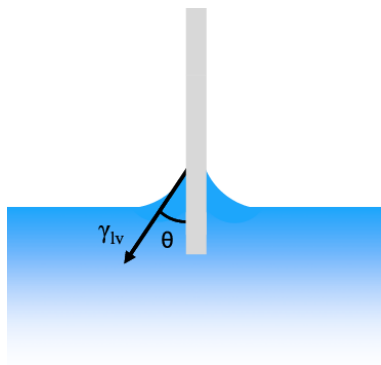


Figure 2.7: Schematic of the Wilhelmy balance method (Yuan and Lee, 2013)

### 2.5.6. Capillary tube

When the inside and outside of a tube are made from the same material the wilhelmy balance method can also be used. The tube gives an additional capillary rise to the liquid, see Figure 2.3.

## 2.6. Surface Roughness

All methods mentioned in chapter 2.5 are subject to the effect of surface roughness of the solid used. The roughness of the surface can greatly affect the wettability of the surface and therefore the contact angle measured (Morrow, 1975, Wenzel, 1936). The surface roughness is characterized according to (Wenzel, 1936)

$$\text{roughness factor} = r = \frac{\text{actual surface}}{\text{geometric surface}}, \quad (2.6)$$

where the geometric surface is a theoretical perfectly flat surface. Minimizing the roughness factor by polishing a surface is of great importance for a consistent and accurate measuring of the contact angle.



# 3

## Experimental setup and procedures

The experimental setup and procedures define the consistency and accuracy of the contact angle measurements. In this chapter the experimental setup that has been used is explained as well as the materials and how we measured the results and the performance of the experiment.

### 3.1. Captive Bubble Setup

The captive bubble method from 2.5 was chosen as this would be the most suitable method to measure the contact angle of a hydrogen/brine/rock system at high pressure and temperature. The captive bubble setup is a modified version of the setup used previously by Shojai Kaveh et al., (2014). The schematic of the setup is given in Figure 3.1. The cell comprises of a single steel cell in which a rock sample can be placed and fluids can be injected. Two inlets are placed on the bottom, one is used for injection of brine and the other, placed directly below the rock sample is used for the injection of gas. Extraction of the brine and gas is done from the top of the cell. The pressure in the cell is kept constant through a back-pressure regulator connected to a nitrogen cylinder.

Injection of the brine and hydrogen is carried out using two different Vindum VP1-12K-HC pumps. To create an equal pressure between the brine and hydrogen before the injection of hydrogen, a pressure gauge is installed between between the hydrogen pump and cell. The hydrogen is pumped through a PEEK nozzle with an inner and outer diameter of 0.25 mm and 1.58 mm, respectively. From the nozzle the hydrogen is released on the rock surface. The bubble formed is photographed using a 12.3 megapixel Nikon D90 attached to an endoscope for additional zoom. On the other side a light source with a green filter to help with the image analysis illuminates the cell. The pressure and temperature of the setup is recorded on a computer connected to the system.

### 3.2. Materials

The injected hydrogen has a purity of 99.99 mol%, and is produced by Lindegas. The three different rocks used are Bentheimer Sandstone, Berea Sandstone and Edwards White Limestone. These rocks were sawed from larger blocks to a size of 30 by 12 by 6 mm. The composition of all rock samples have been measured using a FEI quanta feg 650 Scanning Electron Microscope (SEM), the data can be found in appendix D. The Bentheimer sandstone is composed of quartz (95%), feldspar (3%) and clay minerals (2%). The Berea sandstone is composed of quartz (91 %), feldspar (6 %) and clay minerals (3%). The Edwards White Limestone is composed of calcite (>99%)

The surface roughness of all used samples is measured with a Leica 3D microscope with a stereo explore function, as seen in Figure 3.2. The prepared samples are characterized by their  $P_a$  factor, which is the arithmetic mean of the absolute ordinate values within a sampling length. A higher  $P_a$  factor corresponds to a rougher surface. For the experiment, the samples with the lowest  $P_a$  factor are chosen to limit the impact of surface roughness on the measurement and increase the accuracy and repeatability of the experiment. The values for the surface roughness can be found in appendix A.

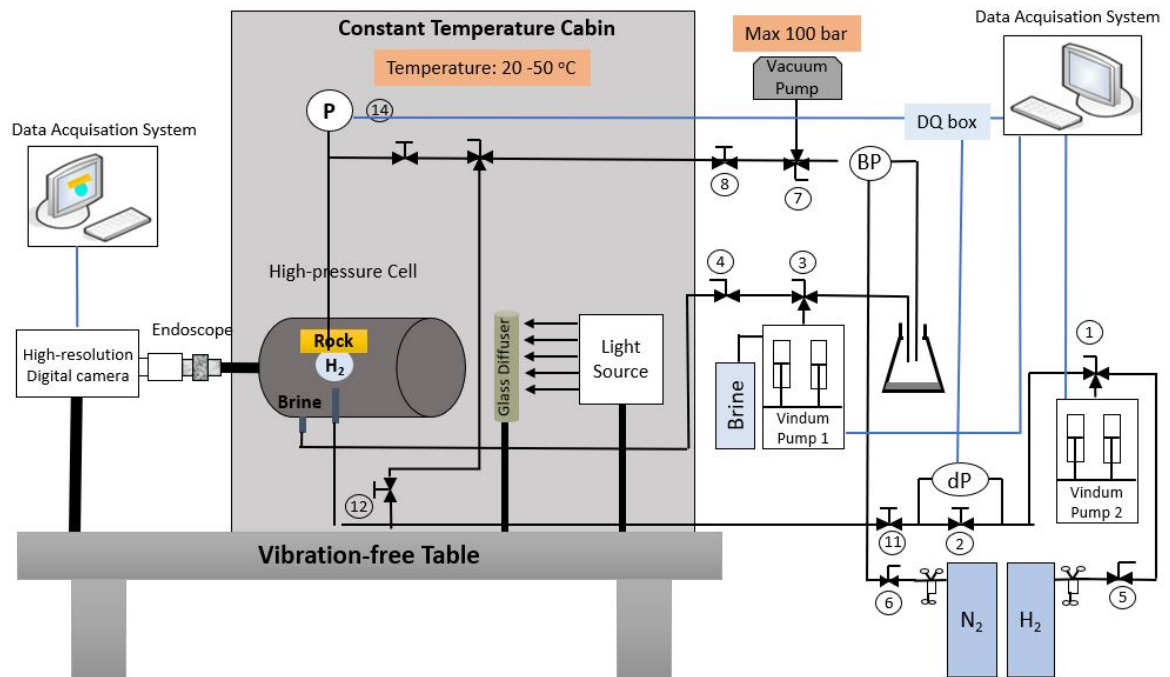


Figure 3.1: Schematic of the experimental setup of the captive bubble cell

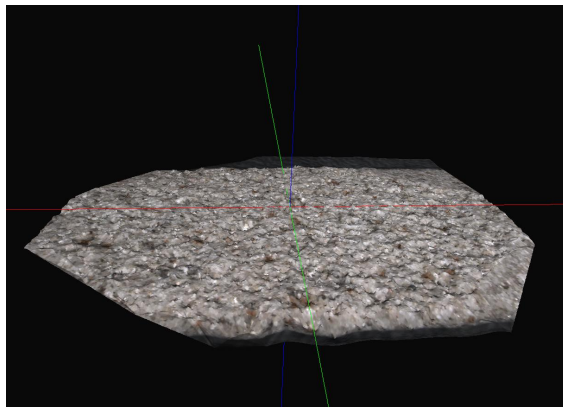


Figure 3.2: Three dimensional view of a Berea rock surface through the Leica 3D microscope. The sample has a  $P_a$  factor of 0.03 mm. Blue, red and green lines give the x,y and z directions used to determine the  $P_a$  value.

### 3.3. Procedure

To start the experiment the cell is filled with brine and brought to the desired pressure and temperature. Then a hydrogen bubble is injected from the nozzle at the bottom of the cell, which rises due to buoyancy and sticks to the rock surface. Images can then be taken with the camera. Due to diffusion and dissolution of the hydrogen into the brine, the bubble reduces in size over time. Therefore, multiple images are taken of one bubble. Images taken will look similar to the one in Figure 3.3.

### 3.4. Image Analysis

To calculate the contact angle of the bubble the in-house MATLAB code from and described by Hashemi et al., May 2021 is used. As seen in Figure 3.4, the image is converted to grey-scale format and cropped to only show the bubble and rock surface. To find the boundary of the bubble, the image is binarized. Tracing the boundary of the bubble, detecting the apex and contact points were followed by fitting the best curve based on the Axisymmetric Drop Shape Analysis-Profile (ADSA-P) technique.

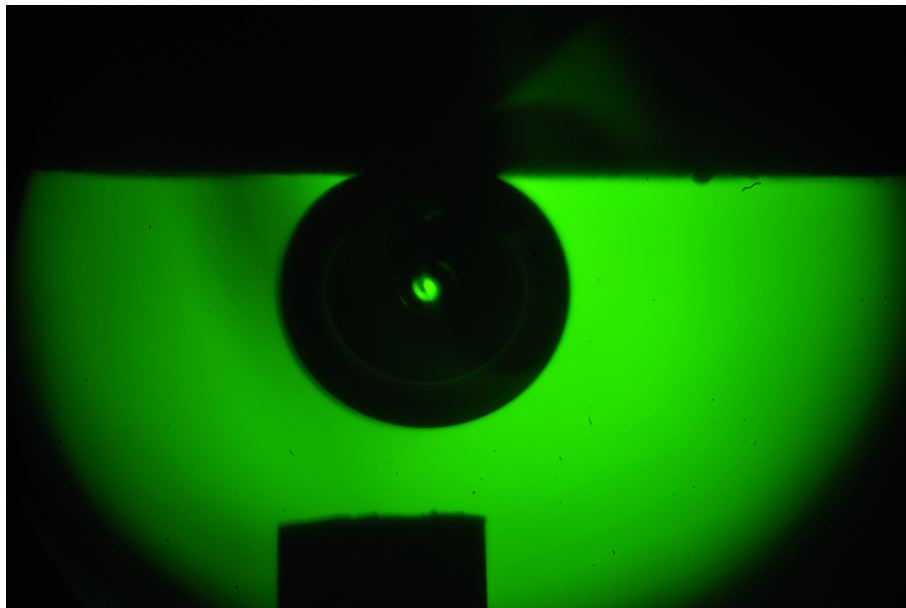


Figure 3.3: Hydrogen bubble image taken at a 5000ppm brine, 70.2 bar and 22.3°C with a Berea sandstone. The bubble and nozzle can be clearly differentiated in black from the brine in green. The flat surface at the top corresponds to the rock surface

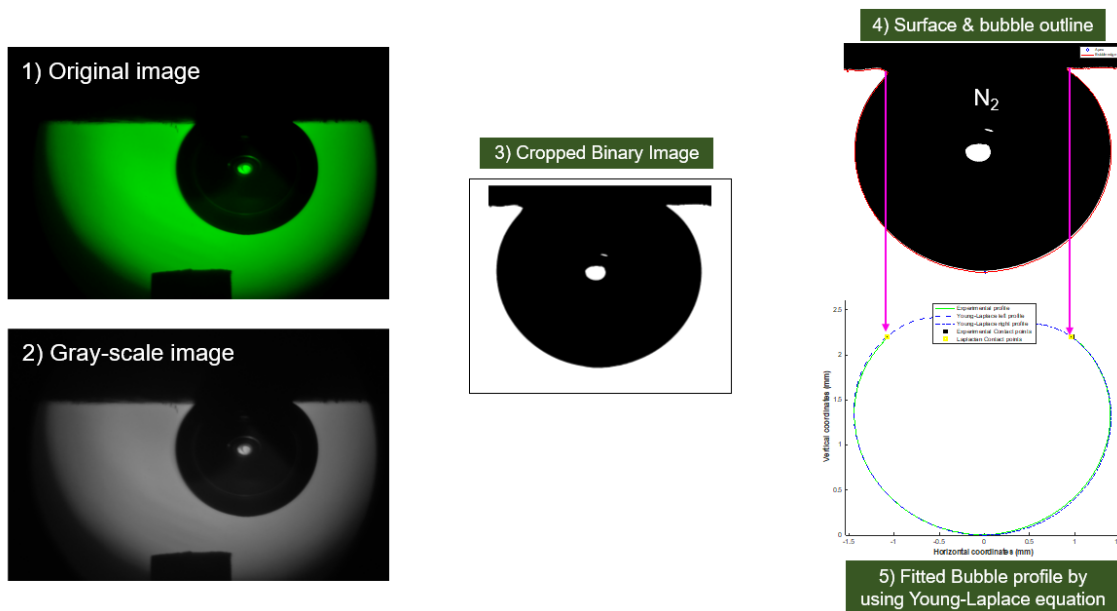


Figure 3.4: Image analysis process to determine the contact angle from the original image (1) to the fitted bubble profile (5) by Hashemi et al., May 2021

This technique fits the best theoretical Laplacian curve on the physical observed bubble interface (Li et al., 1992). The Young-Laplace equation for two fluid phases reads 3.1

$$\Delta P = \gamma \left( \frac{1}{R_1} + \frac{1}{R_2} \right), \tag{3.1}$$

where  $\gamma$  is the interfacial tension and  $R_1$  and  $R_2$  the principle radii of the curvature. Because of the axisymmetry of the bubble the radii are considered equal at the apex. Therefore Equation 3.1 can be written as

$$\Delta P = \frac{2\gamma}{R} \tag{3.2}$$

By considering the gravity as the only external force across the interface, the pressure difference in

equation 3.2 is assumed to be a linear function of the hydrostatic pressure ( $\delta\rho gz$ ) with interception of  $\Delta P_0$  at the reference plane, it becomes,

$$\Delta P = \Delta\rho gz + \Delta P_0 \quad (3.3)$$

As shown in Figure 3.5, the origin of the coordinate system is chosen at the apex point, with the x-axis as a s tangent to the origin and normal to the axis of symmetry, Equation 3.3 is then written as

$$\gamma\left(\frac{1}{R_1} + \frac{\sin(\phi)}{x}\right) = \frac{2\gamma}{R_0} + \Delta\rho gz \quad (3.4)$$

$$\frac{dx}{ds} = \cos(\phi) \quad (3.5)$$

$$\frac{dz}{ds} = \sin(\phi) \quad (3.6)$$

$$\frac{d\phi}{ds} = \frac{2\gamma}{R_0} + \frac{\Delta\rho gz}{\gamma} - \frac{\sin(\phi)}{x} \quad (3.7)$$

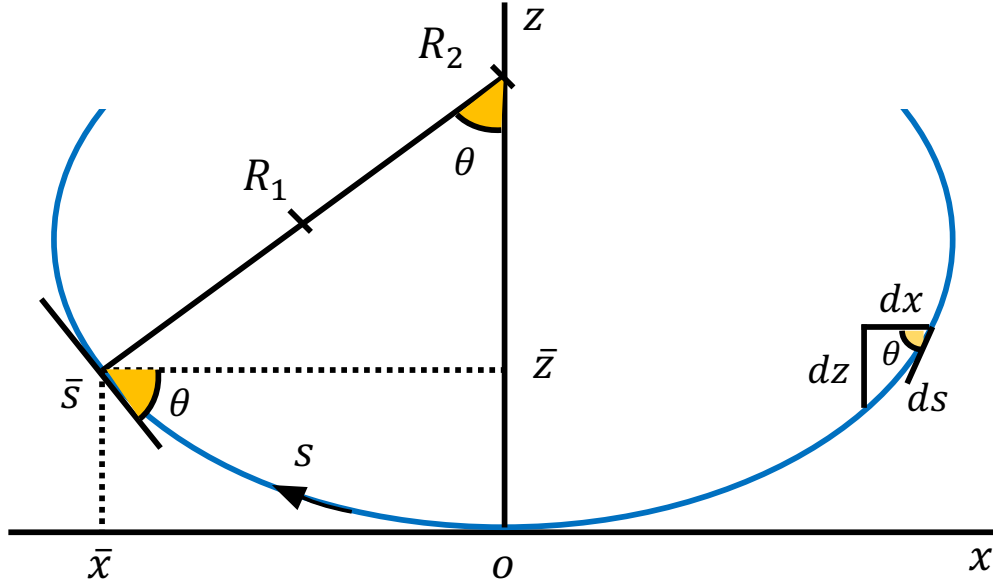


Figure 3.5: Schematic of an axisymmetric drop, modified after Li et al., 1992

Equations 3.5, 3.6 and 3.7 are first order differential equations in terms of the arc length ( $s$ ). These three equations are integrated using the Runge-Kutta numerical approach to find the theoretical Laplacian curve. To find the corresponding contact angle, the objective function is defined to minimize the deviation of the physically-observed curve from the theoretical curve by adjusting the parameters, radius of the curvature at the apex,  $R_0$  and  $\gamma$ . The complete procedure is described extensively by Li et al., 1992. The brine and gas densities were calculated based on the thermodynamic formulation for each pressure and temperature described by Batzle and Wang, 1992.

### 3.5. Setup Calibration

The setup was calibrated with nitrogen and compared to the results of Al-Yaseri et al., 2015. They report a contact angle of  $40.6^\circ \pm 3.9^\circ$  on a smooth alpha-quartz crystal surface. For our Bentheimer sandstone, which mostly consist of quartz, at the same experimental conditions we find a contact angle of  $40.8^\circ \pm 5.6^\circ$ . The full comparison is given in Table 3.1.

Table 3.1: Parameter comparison of the calibration of the setup

Parameters	Al-Yaseri et al., 2015	Our test
Liquid phase	5000 ppm NaCl	5000 ppm NaCl
Gas Phase	N <sub>2</sub>	N <sub>2</sub>
Sample	smooth alpha-quartz crystal	Bentheimer
Pressure (bar)	130	130
Temperature (°C)	60	60
Contact Angle (°)	40.6 ±3.9	40.8 ±5.9

### 3.6. Experimental Conditions

A large number of tests were performed to examine the effects of pressure, temperature, salinity and rock type. A summary of the different cases can be found in Table 3.2.

Table 3.2: Experimental conditions used during the Hydrogen/Brine/Rock experiment

Gas phase	Rock Phase	Brine phase (ppm NaCl)	Temperature (°C)	Pressure (bar)
H <sub>2</sub>	Bentheimer	0	[20, 30, 40, 50]	[20, 50, 70, 100]
		5000	[20, 30, 40, 50]	[20, 50, 70, 100]
		50000	30	[20, 50, 70, 100]
		Synthetic Seawater (Jones et al., 2016)	30	[20, 50, 70, 100]
	Berea	0	[20, 30, 40, 50]	[20, 50, 70, 100]
		5000	[20, 30, 40, 50]	[20, 50, 70, 100]
	Edwards White	0	[20, 30, 50]	[20, 50, 70, 100]
		5000	[20, 30]	[20, 50, 70, 100]

#### 3.6.1. Experimental time

Experiments take around 1.5 to 2 hours to complete. Bringing the cell to the correct pressure and making sure it is stable takes 15 minutes with another 15 minutes required for slow injection of gas. Once a bubble is formed, it is dependent on the bubble size how long it takes to dissolve while photographing the bubble. During this time, the pressure should be monitored to secure a steady state in the cell. This allows for 4 experiments at different pressures, but the same temperature and salinity to take place during a single day.



## Results and Discussion

Throughout the experiments we have looked into four different parameters from Table 3.2, the pressure, temperature, salinity and rock composition. The effects of these parameters will be discussed in this chapter.

Throughout all experiments we find a static contact angle between 25° and 40°. All measurements can be found in appendix B.

### 4.1. Bubble Size

Due to dissolution and diffusion of hydrogen into the brine the size of the bubble changes over time. It was noted that with a decrease in bubble size, the contact angle increases. This has also been seen by Shojai Kaveh et al., (2014) for a CO<sub>2</sub>/brine/rock system. To capture this effect, for each test case several images are taken throughout time. An arithmetic average for the contact angle is taken for these measurements with the maximum and minimum values. The results of this process can be seen in Figure 4.1

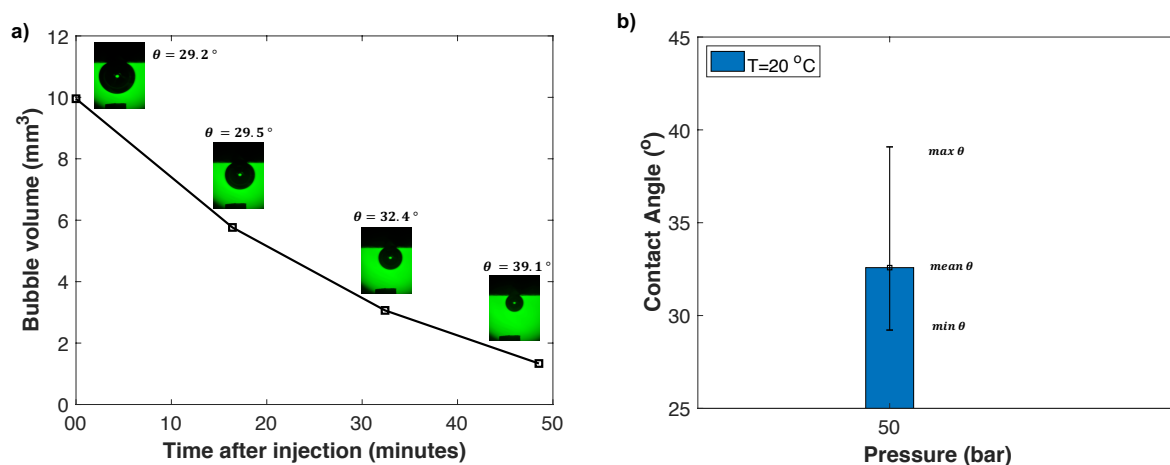


Figure 4.1: Effect of bubble size in the system of hydrogen/water/bentheimer 23.5 °C and 51.2bar. A shows the volume change over time and b the corresponding reported contact angles (Hashemi et al., May 2021)

### 4.2. Pressure and Temperature

Figure 4.2 shows the effect of pressure and temperature on the measurements of the static contact angle in a hydrogen/brine/bentheimer system. All data points regarding pressure and temperature fall within the accuracy of the conducted experiment. Therefore, no correlation between pressure or temperature of the contact angle was found.

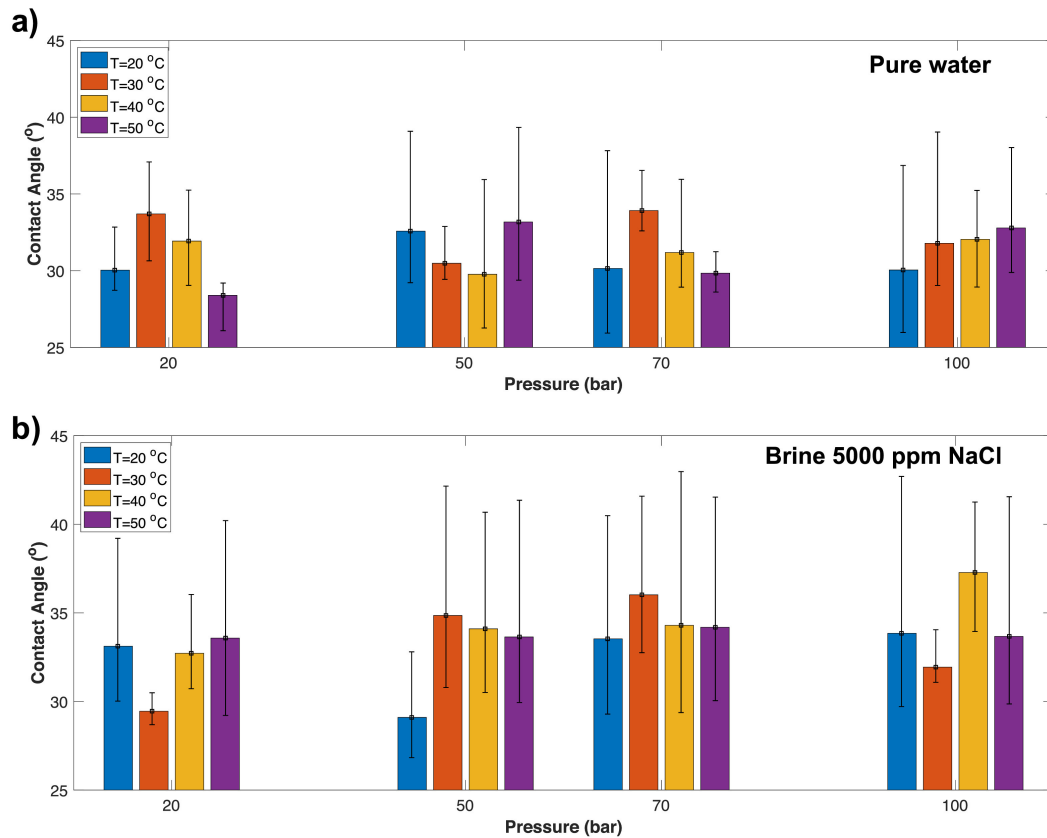


Figure 4.2: Measured static contact angle of hydrogen for a bentheimer sandstone in pure water (a) and 5000 ppm brine (b) at varying pressure and temperature from 3.2

### 4.3. Salinity

The measurements for different brine salinity are shown in Figure 4.3. These measurements also show no discernible change in contact angle due to salinity. This is in contrast to what has been observed in the literature, where it was shown that salinity can alter the wettability (Agbalaka et al., 2009, Jafari and Jung, 2019).

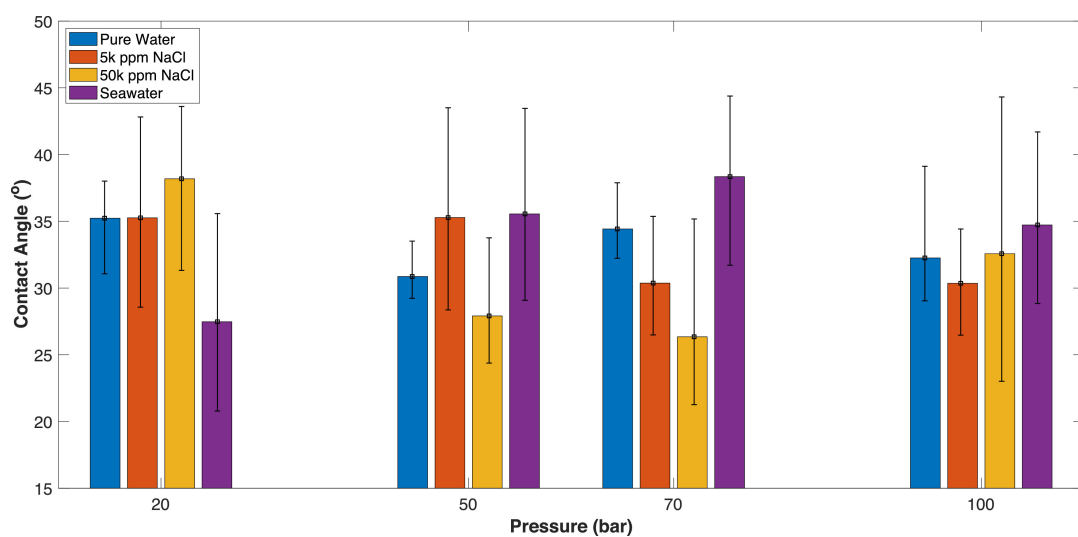


Figure 4.3: Measured static contact angle of hydrogen for a bentheimer sandstone in different brines from Table 3.2 at close to 30 °C

## 4.4. Rock Type

Figure 4.4 shows the contact angle for the different rocks used in the experiment. No differences have been observed for the sandstone and limestone rock samples used in the experiments.

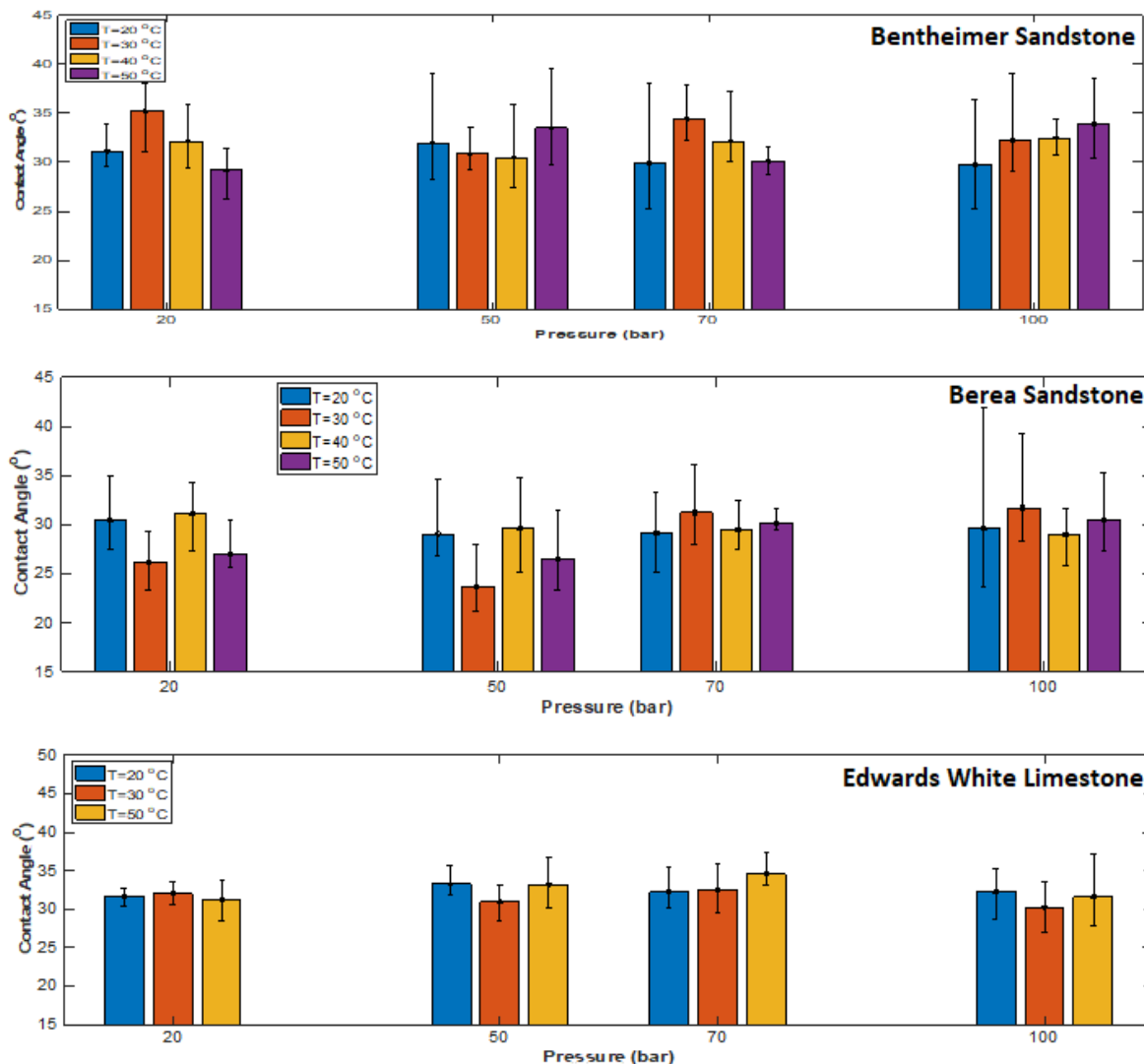


Figure 4.4: Measured static contact angle of hydrogen for a bentheimer sandstone, Berea sandstone and Edwards White Limestone in pure water

## 4.5. Experiment Discussion

During the experiments several problems have occurred, which required changes to the experimental setup or repeats of several experiments.

### 4.5.1. Rock Alteration

The first effect to notice was a small color change on the bentheimer sandstone during the first tests as seen in Figure 4.5. This was most likely deposit of rust from the lines or deposition of copper from the nozzle used for this sample. As this was most likely already present from the start of the experiments, it was decided that we had to repeat the experiment for the bentheimer sandstone. This repetition of the experiment on a new bentheimer sandstone showed that the results were not affected by copper deposit.

After the first experiments with bentheimer and berea sandstone they have been analyzed in the



Figure 4.5: Bentheimer sample with a changed color after experimentation

SEM to see if any alteration to the composition has occurred. From this analysis in appendix D it is seen that the composition has remained the same, but some NaCl has been deposited on the surface. This is likely some crystallization that has occurred after the use of the high salinity brines.

#### **4.5.2. Surface Roughness**

In appendix A it can be seen that the roughness of the Edwards White limestone is a factor 2 lower than that of the Berea and Bentheimer sandstones. This was noted during injection, where the created bubble would start sliding along the rock surface starting at sizes from 1.5 mm. However, this does not always occur and could be an effect of small pressure differences in the cell which result in movement of the bubbles.

# 5

## Conclusions

The wettability of a rock in a hydrogen/brine/rock system plays an important role in the multiphase processes of underground hydrogen storage. We have performed a captive bubble experiment of a hydrogen/brine/rock system in order to quantify the impacts of different parameters. The experimental setup has been validated in a nitrogen/brine/rock system to Al-Yaseri et al., 2015. Throughout an array of different tests different parameters were changed, namely pressure, temperature, salinity and rock composition. All the results indicate water wet conditions with a static contact angle of 21.1 to 43 degrees, with no discernable effect of these parameters on the contact angle. This conclusion of the contact angle of less than 50 ° agrees with the conclusions of Yekta et al., (2018). However, the trend noted by Iglauer et al., (2021) has not been observed in our case. This can be due to differences in measurements technique, experimental conditions and sample preparation. It was also observed that the bubble size affects the contact angle due to a more dominant gravitational force for larger bubbles.

### 5.1. Further Research and Outlook

The captive bubble cell is a flexible experiment in order to find the static contact angle of a gas/water/rock system. In this report we have only looked at experiments in a hydrogen/brine/rock system, however, by substituting different gases the contact angle for those systems can also be easily studied. Another option which has been done before (Ameri et al., 2013) is to study the system with oil saturated rocks. Lastly the experiment setup can be modified to study different behaviours of hydrogen, namely geochemical effect, interfacial tension and solubility.

The results of the experiments of the intrinsic contact angle can be used in pore network models to find the upscaled parameters of capillary pressure and relative permeability, which would be used in continuum scale models.



# 6

## Technical Challenges

With the experience of the initial experiments in a hydrogen/brine/rock system we were interested in other systems and how it would change the behaviour and wettability in other systems.

### 6.1. Aged Rock Samples

In addition to the tests from chapter 3 a plan was made to measure the contact angle in a hydrogen/brine/oil saturated rock system. For these experiments we saturated rock samples in two different oils. A low and high total base number oil (TBN) for 6 and 4 weeks respectively under a constant pressure of 100 bar in a vessel seen in Figure 6.1. From the literature it is known that TBN has a varying effect on the wettability of a system, depend on the TBN of the oil as the brine in the system reacts different to the polar components present in the oil Shabib-Asl et al., 2015.

After saturation a bentheimer sample in high TBN oil was placed in the setup. Quickly it was found that the behaviour of the hydrogen changed when injecting. During injection it is seen that the hydrogen bubble does not release from the PEEK nozzle as seen in Figure 6.2. The idea is that during filling the cell with a brine, some oil releases from the rock sample due to low salinity water flooding. During this process, the oil deposits on the PEEK nozzle, changing the wettability. This change in wettability, causes the buoyancy force to be too small for the bubble to be able to be released from the nozzle. The bubble can be released when it is sufficiently large, but at that moment the bubble is too large to remain on the rock surface and instantly flushes through the cell. Therefore with the current instruments it is not possible to perform the experiment. There would be only one change required, this is changing the nozzle. From Shojai Kaveh et al., (2014) it is known that a brass or copper nozzle has worked in the past for a CO<sub>2</sub>/Brine/Bentheimer system. This change and studying the contact angle of a Hydrogen/Brine/oil-saturated rock system would be useful for understanding the behaviour of Hydrogen in depleted oil reservoirs.

### 6.2. Methane and Methane-Hydrogen Mixtures

During the cyclic process of hydrogen injection, a cushion gas would be used to ensure safety and stability in the reservoir (Hassanpouryouzband et al., 2021). During this process, methane would also be injected into the same reservoir as the hydrogen. During injection and storage Methane and hydrogen would mix and diffuse into each other, creating a mixture in parts of the reservoir. As this would be an important part of hydrogen storage, it would also be important to find the contact angle of Methane/brine/rock and Methane-Hydrogen/Brine/Rock systems. The following scenarios of Table 6.1 were tested.

#### 6.2.1. Experimental Discussion

Due to a few mistakes made during the experiments. It was not possible to gain accurate results of a methane/brine/rock system and therefore these had to be repeated. This is still in progress. However during injection of methane one clear difference to hydrogen can be noted.

During injection of high salinity brine (50000 ppm) the behaviour of the bubbles changes com-

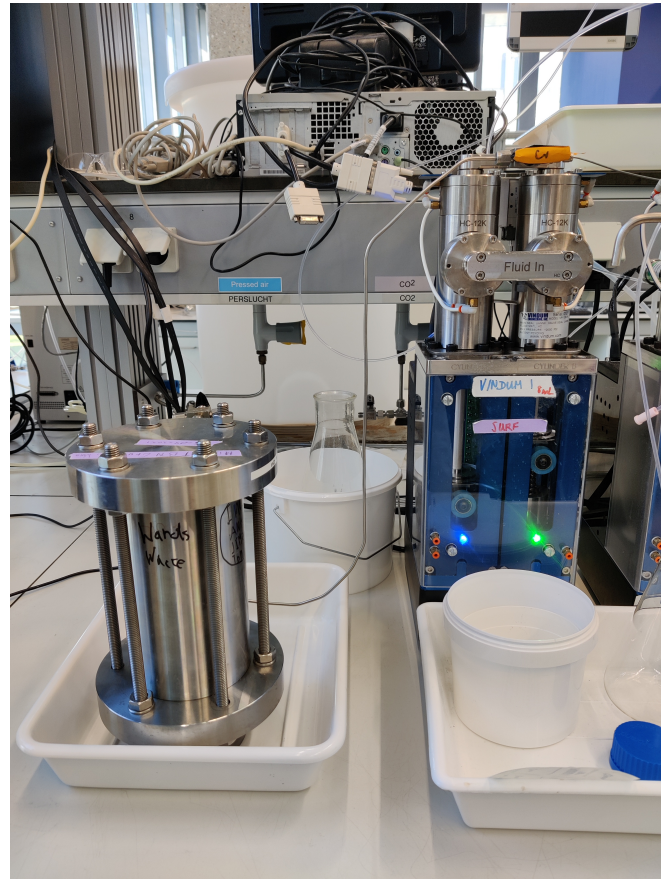


Figure 6.1: Saturation vessel at a pressure of 100 bar with rock samples in oil

pared to low salinity brine or pure water. At these high salinities, the injected bubbles do not merge into a single large bubble, but stay at their injection size. This makes it more difficult to create a bubble on the rock surface, which can be photographed. This change in behaviour has a possible explanation. It is known that an increase in brine increases the interfacial tension of the bubbles (Kashefi et al., 2016). This in turn causes an increase in energy required for the bubbles to overcome the interfacial tension and merge into each other.

## 6.3. Captive Bubble Setup Performance

### 6.3.1. Nozzle

The original material for the nozzle was copper. Due to corrosion, the size and shape of the nozzle had changed over the years that the setup was not in use. With the first experiments, we noticed that this could be a long term problem, therefore we replaced the nozzle with PEEK. PEEK was chosen as it was easily available and would not react with the hydrogen and would not corrode over time.

### 6.3.2. Gas Line Volume

An additional benefit of using PEEK was that part of the line from the pressure gauge to the nozzle could be made from one continuous line. This reduced the volume inside the line from the pump to nozzle. This volume reduction helped when controlling the injection of a single hydrogen bubble into the cell. However it was still difficult to release only a small bubble into the cell by controlling the flow from the pump. To be able to control the release of a single bubble, a needle valve was installed at the start of the PEEK line. The idea of this valve was that turning the needle would induce a small volume change in the line. This change in volume was just enough to release only a single bubble into the setup.

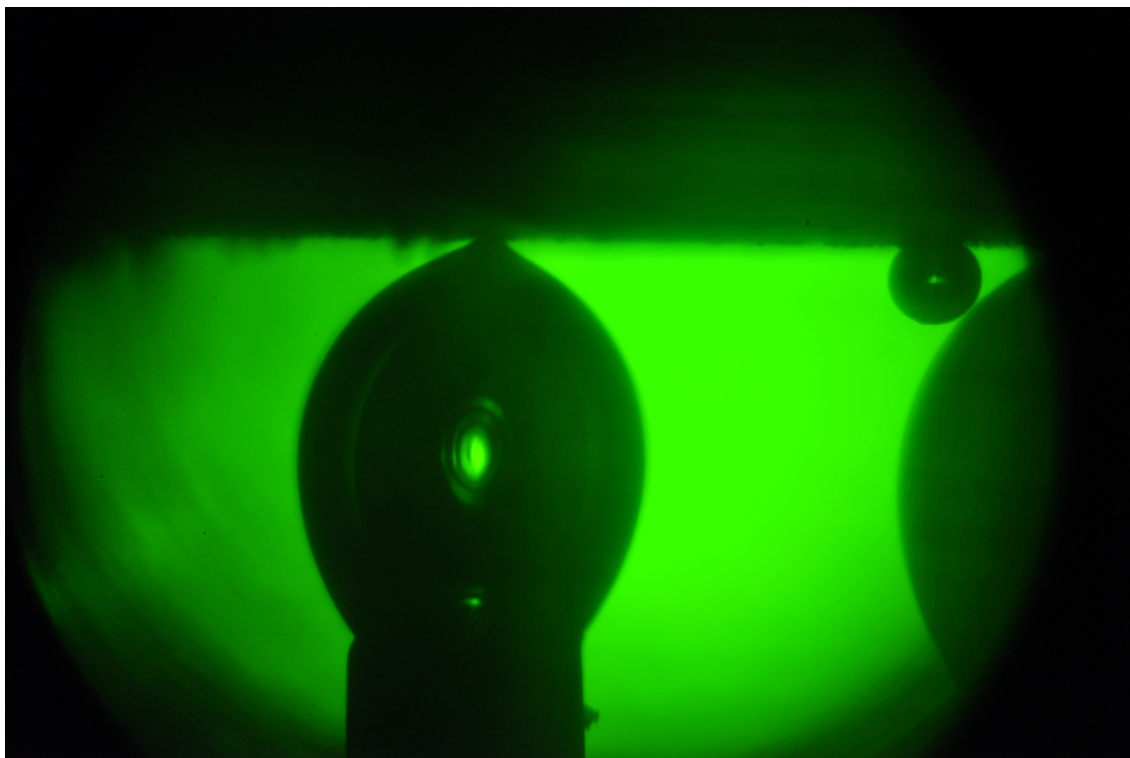


Figure 6.2: Hydrogen bubble with a saturated bentheimer sandstone attached to the PEEK nozzle

Table 6.1: Different test cases used throughout the experiment for a Methane/brine/rock and Methane-Hydrogen/Brine/Rock systems

Rock Sample	Gas (Mole%)	Brine Salinity (ppm)	Temperature (°C)	Pressure (bar)
Bentheimer Sandstone	Methane	0	[30,50]	[20, 50, 70, 100]
		5000	[30,50]	[20, 50, 70, 100]
	50-50 CH <sub>4</sub> -H <sub>2</sub>	0	[30,50]	[20, 50, 70, 100]
		5000	[30,50]	[20, 50, 70, 100]
	80-20 CH <sub>4</sub> -H <sub>2</sub>	0	[30,50]	[20, 50, 70, 100]
		5000	[30,50]	[20, 50, 70, 100]
	20-80 CH <sub>4</sub> -H <sub>2</sub>	0	[30,50]	[20, 50, 70, 100]
		5000	[30,50]	[20, 50, 70, 100]

### 6.3.3. Images

For the image processing the best possible image of the bubble should be captured. This would ideally be a photo containing only a single bubble, focused to clarify the edges of the bubble and the rock surface, as seen in Figure 3.3. However while using the setup it is not always possible to create the perfect image. Things to watch out for are seen in Figure 6.3. These are:

1. There are smaller bubbles surrounding the contact point of the bubble with the rock surface.
2. Images focused on the nozzle.

The first problem can be solved during the injection of the gas by carefully controlling the volume that is injected by using the needle valve. If however, there are still some small bubbles surrounding the contact point, waiting for the smaller bubbles to dissolve or dissipate can also work, if they are small enough.

The second problem can easily be solved by looking at the pictures during the experiment and changing the focus of the camera accordingly.

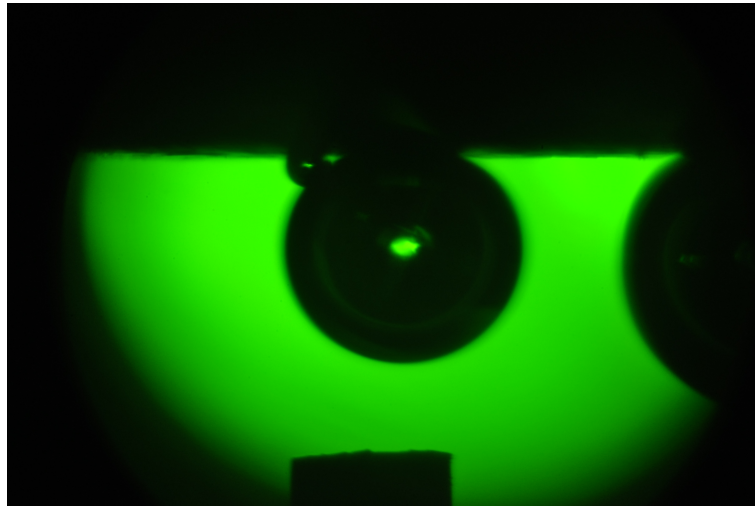


Figure 6.3: Hydrogen bubble image taken at a 5000ppm brine, 71.1 bar and 32.7°C with a Bentheimer sandstone.

#### 6.3.4. Rock replacement

Currently, at least two people are required to open the cell, to clean the cell or to replace the rock sample. The cell is too heavy for one person to take it out of its holder. To open the bolts is also not possible for only one person. The same is true for closing the cell and placing it back into the holder. Unfortunately, The only way for the rock sample to be replaced is by fully opening the cell. The whole process for replacing the rock sample, which includes closing the cell, performing a leakage test and filling the cell with a brine takes a minimum of a full day of work time. For a revision of the pendant drop cell it would be very useful to dramatically decrease the weight and size of the cell. This is so that a single person would be able to open the cell for cleaning. It would also be very useful to create a better way to replace rock sample without having to remove all bolts from the cell casing. This would help with efficiency as it would not be necessary to do a full leakage test every time the cell rock sample was changed.

#### 6.3.5. Flushing Mechanism

In one of the versions of the experimental setup, the line of the brine pump was connected to the gas line through a series of valves. The idea of this would be to flush brine through the nozzle in order to remove any bubble from the rock surface in order to start with a clear sample. This function was later removed because with the brine a small amount of rust would be flushed with it, possibly depositing on and contaminating the rock sample.

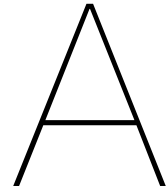
# Bibliography

- Agbalaka, C., Dandekar, A., Patil, S., Khataniar, S., & Hemsath, J. (2009). Coreflooding studies to evaluate the impact of salinity and wettability on oil recovery efficiency. *Transport in Porous Media*, 76, 77–94. <https://doi.org/10.1007/s11242-008-9235-7>
- Al-Yaseri, A., Sarmadivaleh, M., Saeedi, A., Lebedev, M., Barifcani, A., & Iglauer, S. (2015). N<sub>2</sub> co<sub>2</sub> nacl brine interfacial tensions and contact angles on quartz at co<sub>2</sub> storage site conditions in the gippsland basin, victoria/australia. *Journal of Petroleum Science and Engineering*, 129, 58–62. <https://doi.org/10.1016/j.petrol.2015.01.026>
- Ameri, A., Kaveh, N. S., Rudolph, E. S. J., Wolf, K. H., Farajzadeh, R., & Bruining, J. (2013). Investigation on interfacial interactions among crude oil–brine–sandstone rock–co<sub>2</sub> by contact angle measurements. *Energy & Fuels*, 27(2), 1015–1025. <https://doi.org/10.1021/ef3017915>
- Anderson, W. (1987a). Wettability Literature Survey Part 5: The Effects of Wettability on Relative Permeability. *Journal of Petroleum Technology*, 39(11), 1453–1468. <https://doi.org/10.2118/16323-PA>
- Anderson, W. (1987b). Wettability Literature Survey- Part 4: Effects of Wettability on Capillary Pressure. *Journal of Petroleum Technology*, 39(10), 1283–1300. <https://doi.org/10.2118/15271-PA>
- Batzle, M., & Wang, Z. (1992). Seismic properties of pore fluids. *GEOPHYSICS*, 57(11), 1396–1408. <https://doi.org/10.1190/1.1443207>
- Blunt, M. J. (2017). *Multiphase flow in permeable media: A pore-scale perspective*. Cambridge University Press.
- Bradford, S. A., Abriola, L. M., & Leij, F. J. (1997). Wettability effects on two- and three-fluid relative permeabilities. *Journal of Contaminant Hydrology*, 28(1), 171–191. [https://doi.org/https://doi.org/10.1016/S0169-7722\(97\)00024-7](https://doi.org/10.1016/S0169-7722(97)00024-7)
- Brown, H. W. (1951). Capillary Pressure Investigations. *Journal of Petroleum Technology*, 3(03), 67–74. <https://doi.org/10.2118/951067-G>
- Dusseault, M., Bachu, S., & Rothenburg, L. (2004). Sequestration of CO<sub>2</sub> in Salt Caverns. *Journal of Canadian Petroleum Technology*, 43(11). <https://doi.org/10.2118/04-11-04>
- Eccles, J. K., Pratson, L., Newell, R. G., & Jackson, R. B. (2009). Physical and economic potential of geological co<sub>2</sub> storage in saline aquifers. *Environmental Science & Technology*, 43(6), 1962–1969. <https://doi.org/10.1021/es801572e>
- Evans, C., & Guerrero, E. (1979). *Theory And Application Of Capillary Pressure* (Vol. All Days) [SPWLA-1979-MM].
- Hashemi, L., Blunt, M., & Hajibeygi, H. (April, 2021). Pore-scale modelling and sensitivity analyses of hydrogen-brine multiphase flow in geological porous media. *Scientific Reports*, 11(1), 8348. <https://doi.org/10.1038/s41598-021-87490-7>
- Hashemi, L., Glerum, W., Farajzadeh, R., & Hajibeygi, H. (May 2021). Contact angle measurement for hydrogen/brine/sandstone system using captive-bubble method relevant for underground hydrogen storage. *Advances in Water Resources*, 154, 103964. [https://doi.org/https://doi.org/10.1016/j.advwatres.2021.103964](https://doi.org/10.1016/j.advwatres.2021.103964)
- Hassanpouryouzband, A., Joonaki, E., Edlmann, K., & Haszeldine, R. S. (2021). Offshore geological storage of hydrogen: Is this our best option to achieve net-zero? *ACS Energy Letters*, 6(6), 2181–2186. <https://doi.org/10.1021/acseenergylett.1c00845>
- Heinemann, N., Alcalde, J., Miocic, J. M., Hangx, S. J. T., Kallmeyer, J., Ostertag-Henning, C., Hassanpouryouzband, A., Thaysen, E. M., Strobel, G. J., Schmidt-Hattenberger, C., Edlmann, K., Wilkinson, M., Bentham, M., Stuart Haszeldine, R., Carbonell, R., & Rudloff, A. (2021). Enabling large-scale hydrogen storage in porous media – the scientific challenges. *Energy Environ. Sci.*, 14, 853–864. <https://doi.org/10.1039/D0EE03536J>
- Honarpour, M., & Mahmood, S. (1988). Relative-Permeability Measurements: An Overview. *Journal of Petroleum Technology*, 40(08), 963–966. <https://doi.org/10.2118/18565-PA>

- Iglauer, S., Ali, M., & Keshavarz, A. (2021). Hydrogen wettability of sandstone reservoirs: Implications for hydrogen geo-storage [e2020GL090814 2020GL090814]. *Geophysical Research Letters*, 48(3), e2020GL090814. <https://doi.org/https://doi.org/10.1029/2020GL090814>
- Jafari, M., & Jung, J. (2019). Salinity effect on micro-scale contact angles using a 2d micromodel for geological carbon dioxide sequestration. *Journal of Petroleum Science and Engineering*, 178, 152–161. <https://doi.org/https://doi.org/10.1016/j.petrol.2019.03.033>
- Jones, S., Laskaris, G., Vincent-Bonnieu, S., Farajzadeh, R., & Rossen, W. (2016). Effect of surfactant concentration on foam: From coreflood experiments to implicit-texture foam-model parameters. *Journal of Industrial and Engineering Chemistry*, 37, 268–276. <https://doi.org/https://doi.org/10.1016/j.jiec.2016.03.041>
- Juez-Larré, J., van Gessel, S., Dalman, R., Remmelts, G., & Groenenberg, R. (2019). Assessment of underground energy storage potential to support the energy transition in the netherlands. *First Break*, 37(7), 57–66. <https://doi.org/https://doi.org/10.3997/1365-2397.n0039>
- Kashefi, K., Pereira, L. M., Chapoy, A., Burgass, R., & Tohidi, B. (2016). Measurement and modelling of interfacial tension in methane/water and methane/brine systems at reservoir conditions. *Fluid Phase Equilibria*, 409, 301–311. <https://doi.org/https://doi.org/10.1016/j.fluid.2015.09.050>
- Larter, S. R., & Aplin, A. C. (1995). Reservoir geochemistry: Methods, applications and opportunities. *Geological Society, London, Special Publications*, 86(1), 5–32. <https://doi.org/10.1144/GSL.SP.1995.086.01.02>
- Li, D., Cheng, P., & Neumann, A. (1992). Contact angle measurement by axisymmetric drop shape analysis (adsa). *Advances in Colloid and Interface Science*, 39, 347–382. [https://doi.org/https://doi.org/10.1016/0001-8686\(92\)80065-6](https://doi.org/https://doi.org/10.1016/0001-8686(92)80065-6)
- Macdougall, G., Ockrent, C., & Kendall, J. P. ((1942)). Surface energy relations in liquid/solid systems i. the adhesion of liquids to solids and a new method of determining the surface tension of liquids. *Proceedings of the Royal Society of London. Series A. Mathematical and Physical Sciences*, 180(981), 151–173. <https://doi.org/10.1098/rspa.1942.0031>
- Morrow, N. R. (1975). The Effects of Surface Roughness On Contact: Angle With Special Reference to Petroleum Recovery. *Journal of Canadian Petroleum Technology*, 14(04). <https://doi.org/10.2118/75-04-04>
- Morrow, N. R. (1990). Wettability and Its Effect on Oil Recovery. *Journal of Petroleum Technology*, 42(12), 1476–1484. <https://doi.org/10.2118/21621-PA>
- Owens, W., & Archer, D. (1971). The Effect of Rock Wettability on Oil-Water Relative Permeability Relationships. *Journal of Petroleum Technology*, 23(07), 873–878. <https://doi.org/10.2118/3034-PA>
- RVO. (2019). The effects of hydrogen injection in natural gas networks for the dutch underground storages.
- Schelfaut, S. (2021). Netbeheerders al maanden bezig met zonsverduisening: Gaat het licht uit? *Algemeen Dagblad*. Retrieved July 19, 2017, from <https://www.ad.nl/economie/netbeheerders-al-maanden-bezig-met-zonsverduistering-gaat-het-licht-uit~a68fb2a6/>
- Shabib-Asl, A., Ayoub, M., Saaid, I., & Valentim, P. (2015). Experimental investigation into effects of crude oil acid and base number on wettability alteration by using different low salinity water in sandstone rock. *Journal of the Japan Petroleum Institute*, 58, 228–236. <https://doi.org/10.1627/jpi.58.228>
- Shojai Kaveh, N., Rudolph, E. S. J., van Hemert, P., Rossen, W. R., & Wolf, K.-H. ((2014)). Wettability evaluation of a co2/water/bentheimer sandstone system: Contact angle, dissolution, and bubble size. *Energy & Fuels*, 28(6), 4002–4020. <https://doi.org/10.1021/ef500034j>
- Wenzel, R. N. (1936). Resistance of solid surfaces to wetting by water. *Industrial & Engineering Chemistry*, 28(8), 988–994. <https://doi.org/10.1021/ie50320a024>
- Yekta, A. E., Manceau, J.-C., Gaboreau, S., Pichavant, M., & Audigane, P. (2018). Determination of hydrogen–water relative permeability and capillary pressure in sandstone: Application to underground hydrogen injection in sedimentary formations. *Transport in Porous Media*, 122(2), 333–356.
- Yuan, Y., & Lee, T. R. (2013). Contact angle and wetting properties. In G. Bracco & B. Holst (Eds.), *Surface science techniques* (pp. 3–34). Springer Berlin Heidelberg. [https://doi.org/10.1007/978-3-642-34243-1\\_1](https://doi.org/10.1007/978-3-642-34243-1_1)

- 
- Zivar, D., Kumar, S., & Foroozesh, J. (2021). Underground hydrogen storage: A comprehensive review [Hydrogen Separation, Production and Storage]. *International Journal of Hydrogen Energy*, 46(45), 23436–23462. <https://doi.org/https://doi.org/10.1016/j.ijhydene.2020.08.138>





## Rock sample surface properties

In the table images below, the properties and pictures of the rock samples used can be found

Table A.1: Surface roughness values measured using the Leica 3D stereo explorer

Rock Type	$P_a$ (mm)	Usage	Figure
Bentheimer	0.032	Initial hydrogen tests	NA
Bentheimer	0.031	Repeat hydrogen test	A.1
Berea	0.025	Initial hydrogen tests	A.2
Edwards White	0.011	Initial hydrogen tests	A.3
Bentheimer	0.03	Initial methane tests	A.4
Bentheimer	0.027	Repeat methane tests	A.5



Figure A.1: Bentheimer sandstone used during the repeat test with hydrogen



Figure A.2: Berea sandstone used during the initial test with hydrogen



Figure A.3: Edwards White limestone used during the initial test with hydrogen



Figure A.4: Bentheimer sandstone used during the initial test with methane and methane-hydrogen mixtures



Figure A.5: Bentheimer sandstone used during the repeat test with methane and methane-hydrogen mixtures



# B

## Measurements

The following tables includes all measurements at the experimental conditions.

### B.1. Hydrogen/Brine/Bentheimer

Table B.1: Contact angle values of hydrogen/pure water/Bentheimer.

Test No.	Temp. (°C)	Press. (bar)	$\vartheta_{ave}$ (°)	$\vartheta_{range}$ (°)	Vol. <sub>ave</sub> (mm <sup>3</sup> )	Vol. <sub>range</sub> (mm <sup>3</sup> )
1 T~20°C	22.3	20.3	30	[28.7, 32.8]	4.56	[2.36, 7.05]
	23.5	50.2	32.6	[29.2, 39.1]	5.49	[1.34, 9.96]
	23.4	70.7	31.1	[25.9, 37.8]	3.93	[1.45, 9.10]
	23.9	100.5	30	[26.0, 36.9]	4.05	[1.48, 7.36]
2 T~30°C	31.9	22	33.7	[30.6, 37.1]	3.48	[2.21, 4.66]
	32.5	51.8	30.5	[29.4, 32.9]	3.09	[2.20, 3.66]
	32.8	71.5	33.9	[32.6, 36.5]	3.39	[2.38, 4.48]
	33.2	100.5	31.7	[29.0, 39.0]	5.27	[1.93, 9.49]
3 T~40°C	39.5	20.3	31.9	[29.0, 35.3]	5.09	[2.61, 8.38]
	39.9	50.2	29.8	[26.3, 35.9]	7.42	[2.21, 12.67]
	40.1	72.8	31.2	[28.9, 36.0]	7.04	[2.27, 12.58]
	40.3	100.3	32	[28.9, 35.2]	3.91	[2.32, 6.02]
4 T~50°C	49.1	19.8	28.4	[26.1, 29.2]	7.42	[3.96, 10.65]
	49.2	50.6	33.2	[29.4, 39.3]	4.7	[1.68, 8.39]
	49.3	70.2	29.8	[28.6, 31.2]	4.41	[2.66, 6.33]
	49.3	101.2	32.8	[29.9, 38.0]	4.12	[2.14, 6.35]

Table B.2: Contact angle values of hydrogen/brine (5000 ppm NaCl)/Bentheimer.

Test No.	Temp. (°C)	Press. (bar)	$\vartheta_{ave}$ (°)	$\vartheta_{range}$ (°)	Vol. <sub>ave</sub> (mm <sup>3</sup> )	Vol. <sub>range</sub> (mm <sup>3</sup> )
1 T~20°C	21.3	20	33.1	[30.0, 39.2]	3.99	[1.62, 6.14]
	22.1	51.9	29.1	[26.8, 32.8]	4.08	[1.82, 6.53]
	22.3	71.5	33.5	[29.3, 40.5]	3.76	[1.28, 6.50]
	22.9	100.5	33.9	[29.7, 42.7]	4.13	[1.01, 7.37]
2 T~30°C	38.9	21	29.5	[28.7, 30.5]	4.61	[2.67, 6.55]
	32.2	49.9	34.9	[30.8, 42.2]	3.42	[1.21, 5.77]
	32.7	71.1	36	[32.8, 41.6]	2.8	[1.19, 4.72]
	33.1	98.9	31.9	[31.1, 34.1]	5.59	[2.08, 11.13]
3 T~40°C	38.9	19.6	32.7	[30.7, 36.0]	4.33	[2.45, 6.32]
	39.5	50.8	34.1	[30.5, 40.7]	3.91	[1.44, 6.48]
	39.9	69.9	34.3	[29.4, 43.0]	4.06	[1.16, 7.18]
	40.1	100.1	37.3	[34.0, 41.3]	2.24	[1.34, 3.22]
4 T~50°C	47.4	20.7	33.6	[29.2, 40.2]	4.48	[1.51, 7.78]
	48.3	51.3	33.6	[29.9, 41.4]	4.03	[1.40, 6.45]
	49	70.6	34.2	[30.0, 41.5]	4.34	[1.50, 7.91]
	49.2	100.7	33.7	[29.9, 41.6]	5.7	[1.31, 12.66]

Table B.3: Contact angle values of hydrogen/brine (50,000 ppm NaCl)/Bentheimer.

Test No.	Temp. (°C)	Press. (bar)	$\vartheta_{ave}$ (°)	$\vartheta_{range}$ (°)	Vol. <sub>ave</sub> (mm <sup>3</sup> )	Vol. <sub>range</sub> (mm <sup>3</sup> )
1 T~30°C	31.3	21.1	33.3	[30.4, 36.6]	4.02	[2.10, 6.49]
	31.9	51.4	32.8	[30.3, 32.8]	3.54	[1.66, 5.34]
	33	70.6	31.6	[29.1, 36.7]	3.31	[1.53, 5.38]
	33.3	100.7	34.5	[29.8, 42.5]	3.84	[1.36, 5.77]

Table B.4: Contact angle values of hydrogen/pure water/Bentheimer, repeated tests.

Test No.	Temp. (°C)	Press. (bar)	$\vartheta_{ave}$ (°)	$\vartheta_{range}$ (°)	Vol. <sub>ave</sub> (mm <sup>3</sup> )	Vol. <sub>range</sub> (mm <sup>3</sup> )
1 T~20°C	24.4	23.5	33.7	[30.5, 38.8]	4.88	[1.99, 8.23]
	24.5	50.7	34.8	[30.3, 42.7]	4.05	[1.21, 7.10]
	25	70.4	37.5	[33.4, 44.4]	2.75	[0.96, 4.41]
	25.1	100.7	36.4	[32.4, 41.8]	3.91	[1.29, 8.37]
2 T~40°C	38.8	20.7	35.3	[31.5, 42.8]	3.92	[1.30, 6.64]
	39	48.8	35.3	[32.4, 41.6]	4.21	[1.41, 7.64]
	39.4	70.6	31.1	[27.3, 34.9]	4.47	[1.79, 8.59]
	39.5	99.2	36.2	[31.6, 42.3]	3.58	[1.15, 7.22]

Table B.5: Contact angle values of hydrogen/brine (5000 ppm NaCl)/Bentheimer, repeated tests.

Test No.	Temp. (°C)	Press. (bar)	$\vartheta_{ave}$ (°)	$\vartheta_{range}$ (°)	Vol. <sub>ave</sub> (mm <sup>3</sup> )	Vol. <sub>range</sub> (mm <sup>3</sup> )
1 T~20°C	24	20.3	33.7	[29.7, 40.4]	3.92	[1.53, 5.56]
	24.8	49.4	35.6	[30.8, 42.6]	3.63	[1.18, 6.79]
	24.7	70.9	35.9	[30.5, 43.1]	3.45	[1.08, 5.97]
	24.4	100.9	32.4	[29.5, 37.5]	4.33	[1.54, 7.46]
2 T~40°C	38.7	20.4	31.3	[30.1, 33.3]	4.06	[2.41, 5.91]
	39	51.1	31.69	[27.4, 35.5]	3.89	[1.78, 6.27]
	39.2	70.1	37.4	[34.5, 40.3]	2.54	[1.32, 3.90]
	39.4	100.4	33.6	[30.5, 38.6]	3.51	[1.18, 6.43]

## B.2. Hydrogen/Brine/Berea

Table B.6: Contact angle values of hydrogen/pure water/Berea.

Test No.	Temp. (°C)	Press. (bar)	$\vartheta_{ave}$ (°)	$\vartheta_{range}$ (°)	Vol. <sub>ave</sub> (mm <sup>3</sup> )	Vol. <sub>range</sub> (mm <sup>3</sup> )
1 T~20°C	23.6	20.8	30.4	[27.5, 34.9]	4.96	[1.14, 9.19]
	23.5	50.6	29	[26.8, 34.5]	5	[0.96, 10.74]
	23.7	70.2	29.1	[25.2, 33.3]	5.22	[1.04, 10.28]
	23.9	100.7	29.6	[23.6, 41.9]	4.17	[0.33, 9.51]
2 T~30°C	32.6	19.4	26.1	[23.3, 29.2]	7.65	[1.36, 15.81]
	32.7	50	23.6	[21.1, 27.9]	7.28	[0.79, 14.17]
	32.8	69.3	31.2	[27.9, 36.1]	3.38	[0.54, 7.29]
	33	101.1	31.7	[28.3, 39.3]	3.61	[0.45, 8.59]
3 T~40°C	38.6	21.2	31.1	[27.3, 34.3]	3.01	[0.95, 5.64]
	38.6	51	29.5	[25.1, 34.8]	4.34	[0.94, 9.68]
	38.6	69.4	29.4	[27.4, 32.5]	3.56	[1.17, 7.14]
	38.9	100.7	28.9	[25.8, 31.6]	4.98	[1.52, 10.35]
4 T~50°C	47.6	20.5	27	[25.6, 30.5]	5.57	[0.91, 10.51]
	47.8	49.4	26.4	[23.2, 31.4]	6.49	[0.93, 14.03]
	48.2	70.6	30.1	[29.4, 31.5]	6.68	[5.13, 8.52]
	48.2	99.7	30.5	[27.2, 35.3]	4.55	[0.91, 9.80]

Table B.7: Contact angle values of hydrogen/pure water/Berea, repeated tests.

Test No.	Temp. (°C)	Press. (bar)	$\vartheta_{ave}$ (°)	$\vartheta_{range}$ (°)	Vol. <sub>ave</sub> (mm <sup>3</sup> )	Vol. <sub>range</sub> (mm <sup>3</sup> )
1 T~20°C	24	20.7	30.5	[26.4, 38.6]	5.17	[0.71, 10.29]
	23.7	50.7	29.3	[25.3, 37.5]	5.35	[0.57, 12.05]
	23.5	71.5	26.6	[22.7, 32.8]	5.93	[0.76, 13.08]
	23.5	100.8	24.2	[22.2, 26.5]	9.68	[1.34, 17.42]
2 T~20°C	22.4	19.7	22.8	[20.76, 25.06]	8.66	[2.16, 16.84]
	22.8	49.1	26.4	[23.44, 29.44]	6.02	[1.05, 11.97]

## B.3. Hydrogen/Brine/Edwards White

Table B.8: Contact angle values of hydrogen/pure water/Edwards White

Test No.	Temperature (°C)	Pressure	$\theta_{(ave)}$ (°)	$\theta_{min}$ (°)	$\theta_{max}$ (°)	$\square$ Volume $\square_{(ave)}$	$\square$ Volume $\square_{(min)}$	$\square$ Volume $\square_{(max)}$
						( $\square$ mm $\square^3$ )	( $\square$ mm $\square^3$ )	( $\square$ mm $\square^3$ )
1	22	20.2	31.7	30.4	32.7	1.32	0.93	1.67
	22.4	49.5	33.2	31.9	35.7	1.19	0.67	1.81
	22.5	69.5	32.2	30.2	35.4	1.47	0.78	2.21
	22.6	98.5	32.2	28.7	35.3	1.98	0.66	3.89
2	32.4	20.4	32	30.6	33.6	1.8	0.85	2.95
	32.7	49.7	30.9	28.5	33	2.2	0.9	3.49
	32.9	71.4	32.5	29.6	35.9	2.28	0.66	4.54
	33.1	99.9	30.2	27	33.6	3.57	0.93	6.85
3	48.1	21.1	31.2	28.4	33.8	2.69	1.11	4.25
	48.4	49.6	33.2	30.2	36.6	2.18	0.59	4.55
	48.7	71.4	34.6	33.1	37.3	1.21	0.6	1.85
	49.2	98.9	31.6	27.8	37.1	3.52	0.48	7.71

Table B.9: Contact angle values of hydrogen/brine (5000 ppm NaCl)/Edwards White

Test No.	Temperature (°C)	Pressure	$\theta_{(ave)}$ (°)	$\theta_{min}$ (°)	$\theta_{max}$ (°)	$\square$ Volume $\square_{(ave)}$	$\square$ Volume $\square_{(min)}$	$\square$ Volume $\square_{(max)}$
						( $\square$ mm $\square^3$ )	( $\square$ mm $\square^3$ )	( $\square$ mm $\square^3$ )
1	22.1	20.3	30.3	29.7	31.5	1.74	1.45	1.99
	22.3	51.6	29.8	28.8	31.3	1.75	1.41	2.07
	22.5	71.8	31	29.9	32.9	1.29	0.72	1.94
2	30.4	21	31	29.8	32.9	1.34	0.77	1.93
	30.5	51.5	33.8	32.7	35.1	0.67	0.48	0.84
	30.8	70.9	31.7	30	33.5	0.98	0.8	1.21
	30.8	101.2	32.2	31	33.4	1.34	0.87	1.8



C

Densities

Table C.1: Density values used to calculate the contact angle for bentheimer sandstone

Test No.	Brine	T (oC)	P (bars)	$\rho_w(kg/m^3)$	$\rho_{H_2}(kg/m^3)$
1 (T = ~20)	PureWater	24.5	11.5	996.60	0.93
		22.3	20.3	997.51	1.65
		24.7	30.6	997.41	2.45
		23.5	50.2	998.57	3.98
		22.6	61.6	999.30	4.87
		23.4	70.7	999.51	5.55
		22.8	71.1	999.67	5.59
		23.5	87.6	1000.24	6.80
		23.9	100.5	1000.71	7.73
10 (T = ~20) Repeat		24.4	23.5	997.16	1.89
		24.5	50.7	998.35	4.01
		25.0	70.4	999.11	5.49
2 (T = ~30)		25.1	100.7	1000.42	7.72
		31.9	22	995.12	1.73
		32.5	51.8	996.25	3.99
3 (T = ~40)		32.8	71.5	997.01	5.44
		33.2	100.5	998.15	7.51
		39.5	20.3	992.68	1.56
3 (T = ~40)	39.9	50.2	993.83	3.78	
	40.1	72.8	994.73	5.41	
	40.3	100.3	995.84	7.33	
11 (T = ~40) Repeat	38.8	20.7	992.93	1.59	
	39	48.8	994.08	3.69	
	39.4	70.6	994.88	5.26	
4 (T = ~50)	39.5	99.2	996.07	7.27	
	49.10	19.80	989.17	1.47	
	49.20	50.60	990.44	3.70	
	49.30	70.20	991.23	5.08	
5 (T = ~20)	49.30	101.20	992.53	7.20	
	21.30	20.00	1000.91	1.63	
	22.10	51.90	1002.16	4.13	
	22.30	71.50	1002.99	5.63	
5 (T = ~20) Repeat	22.90	100.50	1004.14	7.76	
	24.00	20.30	1000.29	1.64	
	24.80	49.40	1001.39	3.91	
	24.70	70.90	1002.37	5.54	
6 (T = ~30)	24.40	100.90	1003.77	7.75	
	31.7	21	998.24	1.65	
	32.2	49.9	999.36	3.85	
	32.7	71.1	1000.13	5.41	
7 (T = ~40)	33.1	98.9	1001.21	7.40	
	38.9	19.6	995.91	1.51	
	39.5	50.8	997.05	3.83	
	39.9	69.9	997.73	5.20	
12 (T = ~40) Repeat	40.1	100.1	998.95	7.32	
	38.7	20.4	996.02	1.57	
	39	51.1	997.24	3.86	
	39.2	70.1	997.98	5.23	
8 (T = ~50)	39.4	100.4	999.20	7.36	
	47.40	20.70	992.88	1.55	
	48.30	51.30	993.82	3.76	
	49.00	70.60	994.35	5.11	
9 (T = ~30)	49.20	100.70	995.53	7.16	
	31.30	21.10	1004.18	1.66	
	31.90	51.40	1004.82	3.97	
	33.00	70.60	1004.43	5.37	
	50000PPM NaCl	33.30	100.70	1005.37	7.52

Table C.2: Density values used to calculate the contact angle for berea sandstone

Test No.	Brine	T (oC)	P (bars)	$\rho_w(kg/m^3)$	$\rho_{H_2}(kg/m^3)$
1 (T = ~20)	PureWater	23.6	20.8	997.23	1.68
		23.5	50.6	998.59	4.01
		23.7	70.2	999.42	5.50
		23.9	100.7	1000.72	7.75
		24	20.7	997.13	1.67
		23.7	50.7	998.55	4.02
		23.5	71.5	999.52	5.60
		23.5	100.8	1000.82	7.77
		22.4	19.7	997.46	1.60
		22.8	49.1	998.69	3.91
2 (T = ~30)	PureWater	32.6	19.4	994.80	1.52
		32.7	50	996.11	3.85
		32.8	69.3	996.92	5.28
		33	101.1	998.24	7.56
3 (T = ~40)	PureWater	38.6	21.2	993.02	1.63
		38.6	51	994.30	3.85
		38.6	69.4	995.09	5.19
		38.9	100.7	996.33	7.39
4 (T = ~50)	PureWater	47.60	20.50	989.78	1.53
		47.80	49.40	990.93	3.63
		48.20	70.60	991.68	5.12
		48.20	99.70	992.90	7.12
5 (T = ~20)	5000PPM NaCl	21.60	20.20	1000.85	1.64
		21.80	50.60	1002.17	4.04
		22.30	70.20	1002.93	5.53
		22.60	100.20	1004.20	7.74
6 (T = ~30)	5000PPM NaCl	32.4	21.6	998.06	1.69
		32.4	50.6	999.33	3.90
		32.5	71.4	1000.21	5.44
		32.5	98.7	1001.39	7.40
7 (T = ~50)	5000PPM NaCl	47.30	21.60	992.95	1.61
		47.70	49.60	993.98	3.65
		48.10	69.90	994.68	5.07
		48.50	99.60	995.77	7.10

Table C.3: Density values used to calculate the contact angle for bentheimer sandstone,repeat

Test No.	Brine	T (oC)	P (bars)	$\rho_w(kg/m^3)$	$\rho_{H_2}(kg/m^3)$
4 (T = ~20)	5000PPM NaCl	21.9	20.6	1000.80	1.67
		22.3	49.6	1002.01	3.95
		22.5	70.9	1002.92	5.58
		22.7	99.9	1004.16	7.72
1 (T = ~30)		31.4	19.6	998.27	1.54
		32.1	50.3	999.41	3.88
		32.7	70.2	1000.09	5.34
2 (T = ~40)		33	100.7	1001.32	7.53
		39	19.8	995.89	1.52
		39.3	49.7	997.07	3.75
		39.5	70.7	997.90	5.27
3 (T = ~50)		39.7	100.3	999.10	7.34
		47.6	19.9	992.76	1.49
		48.5	49.1	993.65	3.60
		48.8	71.1	994.45	5.15
1 (T = ~20)		49	100.3	995.60	7.14
	50000PPM NaCl	22.5	19.7	1013.54	1.60
		23.2	50.5	1014.17	4.01
		23.7	72.0	1014.60	5.64
23.9		101.8	1015.70	7.83	
2 (T = ~30)		31	19.8	1004.45	1.56
		31.3	50.1	1005.43	3.88
		31.6	70.2	1005.96	5.36
1 (T = ~30)	31.7	102.4	1007.22	7.68	
	36770 PPM SeaWater	31	20.5	1006.82	1.61
		31.3	50.2	1007.89	3.88
		31.6	69.6	1008.51	5.32
31.6		100.9	1009.85	7.57	

# D

## Scanning Electron Microscope Data

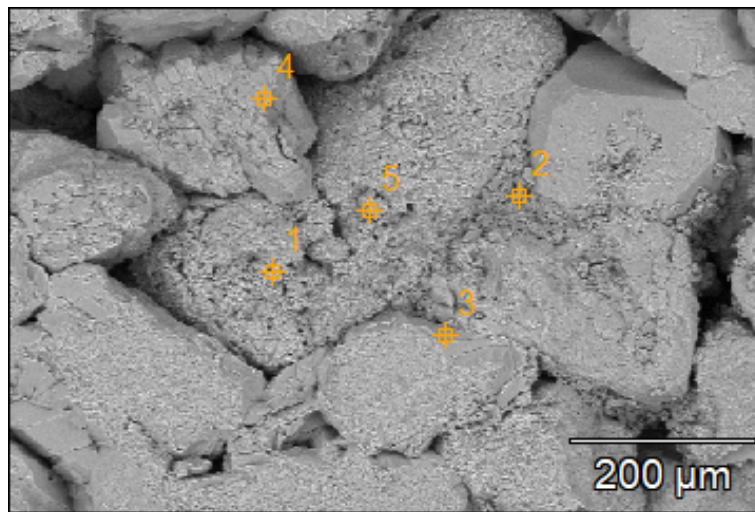


Figure D.1: Pore scale image of a bentheimer sandstone before usage in the experiment

Table D.1: SEM data of a bentheimer sandstone before usage in the experiment

	C	O	Mg	Al	Si	Cl	K	Ca
Unused Bentheimer_pt1	4445	218041	848	23953	327269		1146	
Unused Bentheimer_pt2	2508	116219		28928	264805			543
Unused Bentheimer_pt3	3894	214795		2894	346155			
Unused Bentheimer_pt4	7382	233476		3785	315016	542		14668
Unused Bentheimer_pt5	3436	161860	787	15628	322981		1320	

Table D.2: SEM data of a berea sandstone before usage in the experiment

	C	N	O	F	Na	Mg	Al	Si	P	Cl	K	Ca	Ti	Fe	Zr
Unused Berea_pt1	4163	390	78233			606		103625							166466
Unused Berea_pt2	3449		156416				3662	320467	543		1149				
Unused Berea_pt3	4120		125771		2951		71554	219660	1096	1129	47892			391	
Unused Berea_pt4	2020		59979	0			6604	224212		773	1557	1351	353	657	
Unused Berea_pt5	3499		65508		3008	1730	9897	233165		2181	1566	2769		2134	

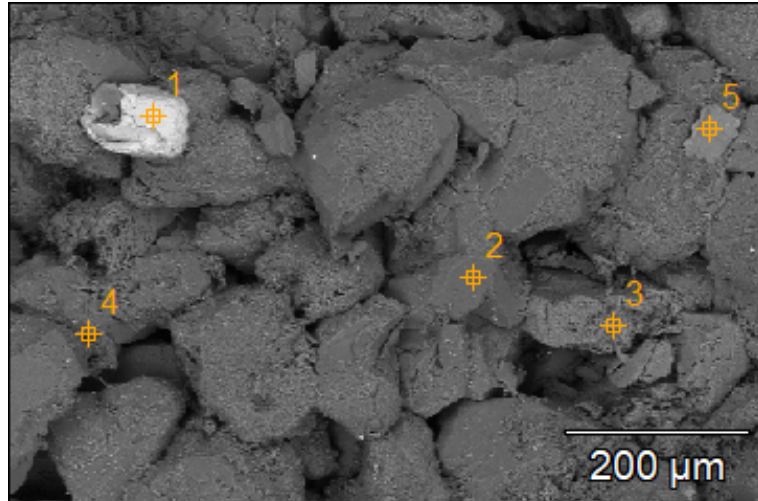


Figure D.2: Pore scale image of a berea sandstone before usage in the experiment

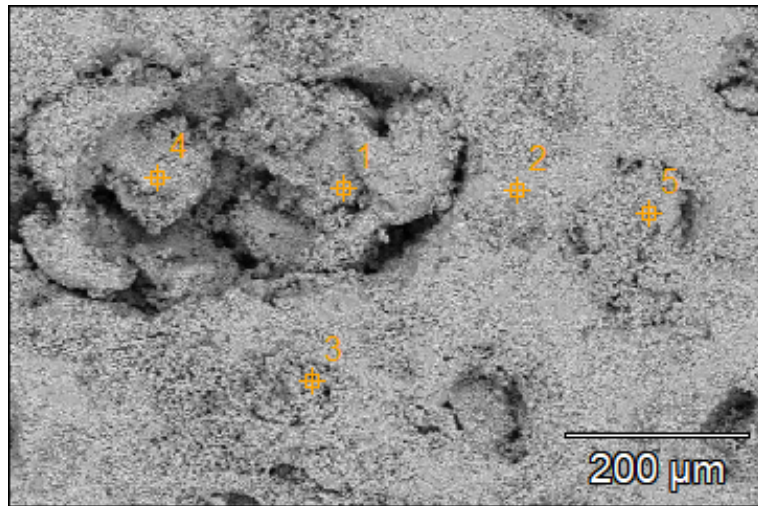


Figure D.3: Pore scale image of an edwards white limestone before usage in the experiment

Table D.3: SEM data of an edwards white limestone before usage in the experiment

	C	O	F	Na	Mg	Al	Si	Cl	K	Ca	Fe
Unused EdwardsWhite_pt1	2575	6265					249			80254	
Unused EdwardsWhite_pt2	23066	49039			1308					147956	
Unused EdwardsWhite_pt3	11518	24197			562					142279	
Unused EdwardsWhite_pt4	24000	73220	0	1412	2546	5533	11564	1036	448	143800	403
Unused EdwardsWhite_pt5	38794	95691			795	325	528	484		149732	

Table D.4: SEM data of an bentheimer sandstone after usage in the experiment

	C	O	F	Na	Al	Si	Cl	K	Mn	Fe	Ni	Cu	Zn	Pd	Re
Used Bentheimer_pt1	385	4057				7948	802				333	686			
Used Bentheimer_pt2	546	5580		162	202	9763	509			255	602	499	181		
Used Bentheimer_pt3	1864	36832			601	20747	52991			1217	3103	27956		0	94
Used Bentheimer_pt4	306	4059			134	8566	1089	112	391	1825	8533	10878	1804		
Used Bentheimer_pt5	5029	223008	0		3384	333871	942			1062	795				

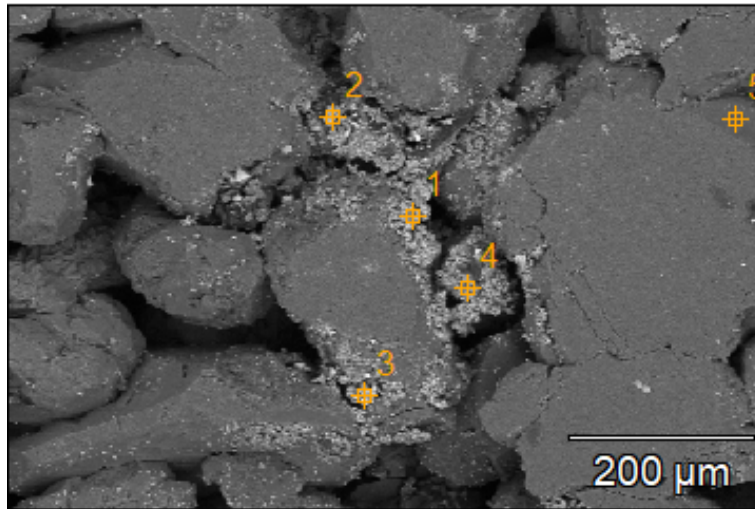


Figure D.4: Pore scale image of a bentheimer sandstone after usage in the experiment

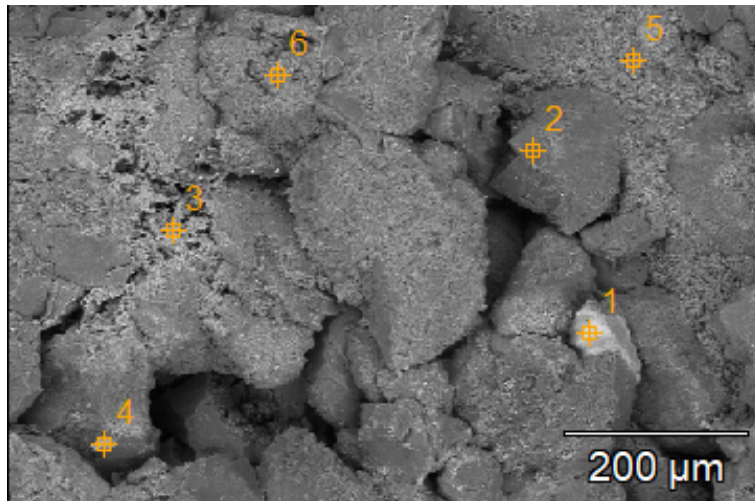


Figure D.5: Pore scale image of a berea sandstone after usage in the experiment

Table D.5: SEM data of an berrea sandstone after usage in the experiment

	C	O	F	Na	Mg	Al	Si	S	Cl	K	Ca	Ti	Mn	Fe	Ni	Cu	Zr	Pd
Used Berea_pt1	3178	47125	1803	87093		3800	90876		87193		611			2499	1003		95259	0
Used Berea_pt2	913	15788	413	25258	397	10602	44097		37939	5231		1312		7559	2791			0
Used Berea_pt3	4415	35806		176329		3082	9779	730	201503		19873			8661	2299			0
Used Berea_pt4	760	11198	0	14669		1766	20385		14394	1117	243		685	724	7408	4507		
Used Berea_pt5	567	9697	0	12278		12525	19695		24206	610				724				0
Used Berea_pt6	1422	17559		119626		3290	105649		152429					595	497			0